THESIS FOR THE DEGREE OF LICENTIATE OF ENGINEERING

Manufacturing and characterization of nanomaterials for low-temperature sintering and electronics thermal management applications

Abdelhafid Zehri

Department of Microtechnology and Nanoscience, MC2
CHALMERS UNIVERSITY OF TECHNOLOGY
Gothenburg, Sweden 2020

Manufacturing and characterization of nanomaterials for low-temperature sintering and electronics thermal management applications

0 Errata

(1) Page I. under Chalmers logo, the page should include ISSN 1652–0769 - Technical Report MC2-432

(2) Page 9, Figure. *The legend should include the text as follow: evolution of number (black) and price (yellow) of transistors, microprocessor power dissipation density (red) and clock frequency (dark green), and power density (light green). Sources : Wikipedia.org (Moore's Law Transistor Count 1971-2018), karlrupp.net (42-years-of-microprocessor-trend-data), iue.tuwien.ac.at (The ITRS and Moore's Law), respectively.*

(3) Page 21. Melting of nanoparticles theory, the queation should be:

$$\Delta Tm=T_{bulk}.2\Delta H_m.\sigma_s\ .\rho_s.r_s$$

To the one who once said, I am sure you will!

Abstract

Nanotechnology is expected to have a significant impact on the long-term development within and across many disciplines. While offering potential improvements in energy efficiency and reduced energy and materials consumption, nanomaterials are at the centre of the cutting-edge technologies and sustainable manufacturing processes era with near half of the products in the next period of 10 years expected to embed nanoscale solutions. The condensed substance of nanosized dimension has shown excellent properties that offer new possibilities due to their surface area to volume ratio. The non-negligible surface energy was proven to induce melting temperature depression, low sintering activation energy and high electronic density that contributes to thermal transport. In this work, we investigate the possibility to take advantage of the advanced nanoscale properties as a sintering aid for low-temperature manufacturing and as thermal dissipation materials for electronics cooling. By combining the high surface energy of the nanomaterial with the tailoring of the local chemical composition, an extra degree of freedom is expected to enable further tuning of their physical and chemical properties. Furthermore, due to the chemical stability of the carbon-based materials and their outstanding physical properties, graphene is explored as a nanoscale coating for nanoparticles and applied herein as a potential nanofiller for nanofluids cooling approach. An additional effort is made to use the graphene/metal composite at a microscale level as high porosity material for heat dissipation.

In this thesis, a novel approach for nanoscale materials production was exploited to manufacture multi-elements alloyed iron nanoparticle. Using spark erosion, low carbon steel nanopowder was produced in order to tune the chemical composition of the nanoparticles in order to combine size effect with composition effect and tailor their performances. A melting depression recorder, while the sintering behaviour of the powder indicated an early activation of the diffusion at temperatures higher than 150°C. The results allow such materials to be used as a sintering aid and lower the sintering temperature of iron powders.

Secondly, graphene coated copper nanoparticles were developed as additives for nanofluids. The nanocomposite fillers of the copper core with multilayers graphene shell were added to water as the base-fluid. The presence of the graphene coating acted as oxidation protection for the metallic particles. Besides, it was found that the presence of the graphene as a local coating on the spherical metallic nanoparticles resulted in a proportional increase in the thermal conductivity of the fluid as the temperature and the concentration of the nanoparticles increased. Such an approach was found promising in the use of graphene-coated nanoparticles as fillers for nanofluids with good heat dissipation.

Finally, graphene has been used as a three-dimensional (3D) foam structure with sintered silver nanoparticles. The sintering of the metallic particles allowed a pressure-free attachment of the high porosity and lightweight material on the back of a chip as a heat sink. The thermal properties of the graphene foam were investigated and found to

reach a thermal conductivity of 319 W/mK. The addition of a layer of coating of silver on the 3D graphene foam material improved further its thermal properties with a 54% enhancement in its effective thermal conductivity. The high porosity fraction was later gradually filled with paraffin as a phase change material. As a result, the maximum temperature of the chip was proportionally lowered and delayed. Most importantly, a CFD model was developed to study the contribution of the secondary microchannels in the heat dissipation process and revealed a positive and non-negligible effect of the additional microporosity present in the case of the graphene foam structure.

Keywords: multi-elements alloyed nanoparticles, sintering aid, graphene coating, graphene foam, heat spreader, nanofluids, phase change materials (PCM).

List of publications

The following papers included in this thesis:

1. Characterisation and Melt Point Depression of Nanosized Low Carbon Alloyed Powder Produced by Arc Discharge. Abdelhafid Zehri, Lilei Ye, Johan Liu. Manuscript under preparation.

2. Graphene-Coated Copper Nanoparticles for Thermal Conductivity Enhancement in Water-Based Nanofluid, Abdelhafid Zehri, Andreas Nylander, Lilei Ye, Johan Liu. CD proceedings of the 22nd European Microelectronics and Packaging Conference & Exhibition (EMPC), Pisa- Italy, 2019, pp. 1-7.

3. High Porosity and Light Weight Graphene Foam Heat Sink and Phase Change Material Container for Thermal Management. Abdelhafid Zehri, Majid Kabiri Samani, Martí Gutierrez Latorre, Andreas Nylander, Torbjörn Nilsson, Yifeng Fu, Nan Wang, Lilei Ye, Johan Liu. Accepted May 11, 2020, Nanotechnology.

Published papers not included in this thesis:

1. *Graphene Related Materials for Thermal Management, Yifeng Fu, Josef Hansson, Ya Liu, Shujing Chen, Abdelhafid Zehri, Majid Kabiri Samani, Nan Wang, Yuxiang Ni, Yan Zhang, Zhi-Bin Zhang, Qianlong Wang, Mengxiong Li, Hongbin Lu, Marianna Sledzinska, Clivia M Sotomayor, Torres Sebastian, Volz Alexander A Balandin, XianG-Fan Xu, Johan Liu, 2D Materials vol. 7 issue (2019) pp: 012001.*
2. *Mechanical Behaviour of Sintered Silver Nanoparticles Reinforced by SiC Microparticles, Xu Long, Zhen Li, Xiuzhen Lu, Hongcun Guo, Chao Chang, Qianran Zhang, Abdelhafid Zehri, Wei Ke, Yao Yao, Lilei Ye, Johan Liu. Materials Science & Engineering, Vol. 744, p. 406-414, 2019.*
3. *Manufacturing Graphene-Encapsulated Copper Particles by Chemical Vapor Deposition in a Cold Wall Reactor. Shujing Chen, Abdelhafid Zehri, Qianlong Wang, Guangjie Yuan, Xiaohua Liu, Nan Wang, and Johan Liu. Chemistry Open 2019; 8(1):58–63.*
4. *Improved Interfacial Bonding Strength and Reliability of Functionalized Graphene Oxide for Cement Reinforcement Applications. Nan Wang, Shuping Wang, Prof. Luping Tang, Lilei Ye, Björn Cullbrand, Abdelhafid Zehri, Behabitu Ergette Tebikachew, Johan Liu. Chemistry - A European Journal. Vol. Chem. Eur. J., 2020, 26,1–9.*
5. *Surface Modification of Graphene for Use as a Structural Fortifier in Water-Borne Epoxy Coatings, Ya Liu, Chao Xia, Abdelhafid Zehri, Lilei Ye, Nan Wang, Boris Zhmud, Hongbin Lu, Johan Liu, MDPI Coatings 2019, 9(11), 754.*
6. *Mechanical Property and Reliability of Bimodal Nano-Silver Paste with Ag-Coated SiC Particles, Qiaoran Zhang, Abdelhafid Zehri, Jiawen Liu, Wei Ke, Shiron Huang, Martí*

Gutierrez Latorre, Nan Wang, Xiuzhen Lu, Cheng Zhou, Weijuan Xia, Yanpei Wu, Lilei Ye, Johan Liu, Soldering and Surface Mount Technology, Vol. 31 No. 4, pp. 193-202.

7. *The Influence of Sintering Process on Thermal Properties of Nano-Silver Paste, Xiuzhen Lu, Qiaoran Zhang, Abdelhafid Zehri, Wei Ke, Shirong Huang, Cheng Zhou, Weijuan Xia, Yanpei Wu, Lilei Ye and Johan Liu, Paper No: 319, Proceedings of the 2018 19th International Conference on Electronic Packaging Technology, 978-1-5386-6386-8/18 2018 IEEE (ICEPT 2018), pp1157-1160, Shanghai-China.*
8. *Low-Temperature Sintering Bimodal Micro Copper-Nano Silver for Electrical Power Devices, Abdelhafid Zehri, Lilei Ye, Johan Liu, Proceedings of the IEEE ESTC Conference, September 2018, Dresden, Germany. IEEE Catalog number: 978-1-5386-6814-6/18.*
9. *Surface Analysis of Iron and Steel Nanopowder, Swathi K. Manchili, Ruslan Shvab, Abdelhafid Zehri, Lilei Ye, Eduard Hryha, Johan Liu, Lars Nyborg, Surface and Interface Analysis (Special Issue), p. 1-6, 20177.*
10. *Fabrication and Characterization of Graphene Based Film, Yuqing Shi, Lilei Ye, Abdelhafid Zehri, Nikolaos Logothetis, Peng Su, Nan Wang, Johan Liu. CD of proceedings of IMAPS Nordic Conference on Microelectronics Packaging, NordPac 2017, Goteborg, Sweden, 18-20 June 2017, p. 162-166, 2016.*
11. *Graphene Fibres: Towards High Mechanical, Thermal and Electrical Properties State of the Art, Abdelhafid Zehri, Josef Hansson, Lilei Ye, Johan Liu, CD of proceedings IMAPS Nordic Annual Conference 2016, Tönsberg-Norway, 5-7 June 2016.*

Contents

Chapter 1: Introduction

1.1 Background

Nanotechnology is expected to have a significant development impact within and across disciplines in research and techno-economic sectors. Due to their tuneable physico-chemical properties, nanomaterials are at the centre of the cutting-edge technologies and manufacturing processes era. The condensed matter of size lower than 100nm has shown intriguing properties compared to their counterparts bulk material with [1]: a lower melting point, higher wettability, enhanced chemical reaction, faster sintering kinetics, higher electrical resistivity, superparamagnetic properties, microwave absorption and localised surface plasmon resonances. They are ideal candidates as catalysts [2], sintering aids [3], microwave absorption magnetic for recording media [4], magnetic fluids [5], conducting ink/paste[6], and additives for heat transfer in fluids [7].

Energy efficiency and environmental issues are becoming of high priorities for future techno- socio and economic developments. Figure 1.a shows the European Commission strategy to reduce the greenhouse gas emission in the next decades where the direct impact of the industrial contribution is estimated to be as high as 22%. Powder metallurgy can already be distinguished as a cost-efficient and environmentally friendly approach for manufacturing due to low material waste and efficient energy use (see Figure 1.b).

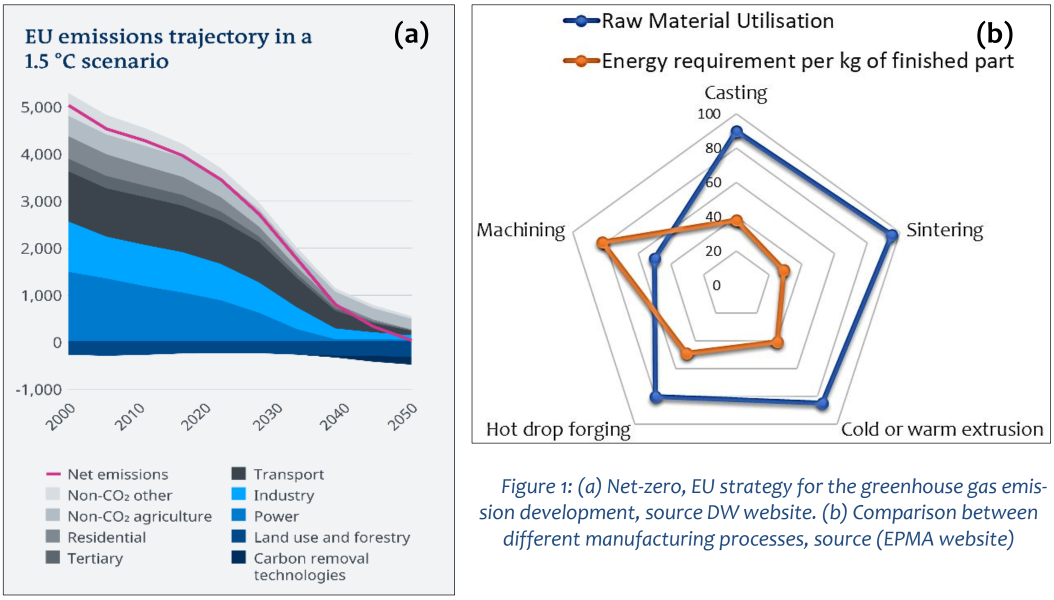

Figure 1: (a) Net-zero, EU strategy for the greenhouse gas emission development, source DW website. (b) Comparison between different manufacturing processes, source (EPMA website)

In order to support the effort to reduce further the impact of the industrial production and technologies, a focus is put into integrating the nanometre materials into the time- and energy-consuming conventional and new manufacturing technologies of powder metallurgy. The high surface area to volume ratio of the nanocrystalline accounts for their high reactivity and driving force for sintering and make them promising candidates. Experimental work on metal and metal oxides nanoparticles validated earlier theories on the non-negligible effect of their high surface energy that results in phase changes and consolidations at lower temperatures. Melting point depression of metallic nanoparticles were found to be highly sensitive to the size and morphology of the particles, especially at values below 20nm [8]. Moreover, work on a broader range of nanoparticles including gold [9], silver [10], copper [11], nickel [10] revealed a higher densification activity at the nanoscale level with an inverse proportional trend with the size of the particle.

In addition to property dependence on size and morphology of the nanoparticles, work has been ongoing to develop novel production and characterisation methods that could allow the development of non-pure nanoparticles. Theoretical approaches have predicted an additional degree of freedom in tuning the physicochemical properties of the nanoparticles through chemical composition tailoring [12], [13]. However, while many reports have emerged recently on production and characterisation of binary nanoalloys [14]–[21], very little progress has been achieved in the area of multi-elements alloyed nanoparticles.

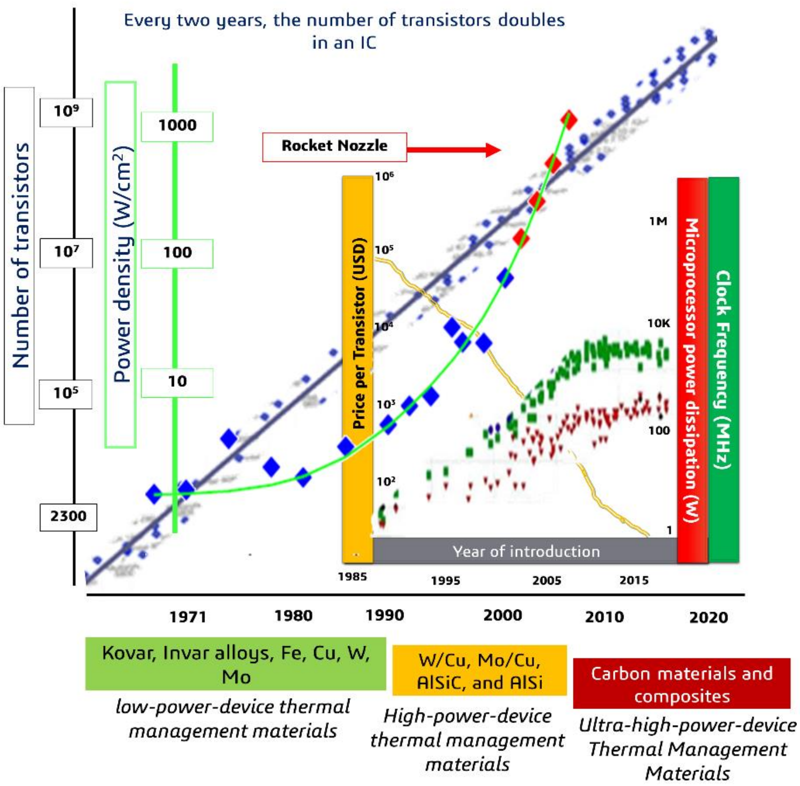

Figure 2: evolution of number and price of transistors, microprocessor power dissipation density and clock frequency, and power density. Sources : Wikipedia.org (Moore's Law Transistor Count 1971-2018), karlrupp.net (42-years-of-microprocessor-trend-data), .iue.tuwien.ac.at (The ITRS and Moore's Law), respectively.

On the other hand, nanoscale thermal management approaches are currently investigated as solutions for the continuous increase in the power densities of the electronic devices to higher than 1000 W/cm^2. As the average cost of a transistor dropped to the billionth of its price, the transistors number, cost, frequency, power densities and heat flux during the last decades kept increasing (see Figure 2). In parallel, a slowdown in the CPUs clock frequencies can be noticed as a direct result of the thermal management issues limitations.

For the future of electronics cooling, metallic nanoparticles and carbon-based materials are expected to have a prominent role due to the high number of atoms and free electrons at the surface and results in an increase in the electronic contribution in physicochemical properties of the material. For instance, high intrinsic properties of graphene have been reported with thermal conductivities up to 5000 W/mK [22]. However, graphene still lacks real case applications in electronics cooling due to integration issues. Conversely, active and passive solutions based on the addition of metallic nanoparticles in fluids requires to solve the issue related to the compatibility of the fluid with the presence of metallic. For instance, many metallic nanoparticles require the addition of additives to protect them from oxidation [23]. Those additions hinder the real potanital of the nanofillers from enhancing the thermal properties of the host fluid.

1.2 Research objective

The effort through this thesis aims at exploring the possibility the produce multi-element alloyed iron nanoparticles using a novel physical approach for nanopowder production. This thesis also sheds light on the possibility of integration of graphene-coating as a protective layer for metallic nanoparticles that finds direct application in cooling fluids. Finally, a real case study of 3-dimensional graphene-based foam coated with sintered silver nanoparticles is explored as a heat sink solution and a phase change container for thermal management. Figure 3 schematizes the focus and progress over the course of this research work

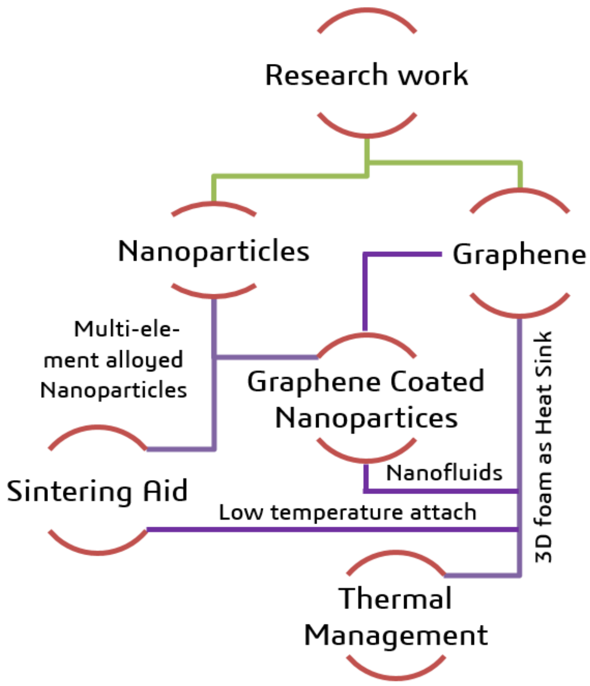

Figure 3: thesis work unreeling

1.3 Outline of the thesis

This thesis is written in four chapters. The first chapter gives a general overview about the role of carbon and nanomaterials and their potential for a multidisciplinary and sustainable development. Chapter two shows the potential of the of production and characterisation of low carbon steel nanopowder as candidates for sintering aid in powder metallurgy technologies. Chapter three is divided into three sections that describes the nature of graphene and its interaction with the substrate, while introducing a novel approach to enhance the thermal properties of the fluids using graphene coated nanoparticles. In the last section, graphene is exploited as a 3D high porosity heat sink and a container for PCM. Chapter four gives brief conclusion about the results achieved in this work.

Chapter 2: Powder metallurgy and nanoparticles for low-temperature sintering

2.1 Introduction

Powder metallurgy (PM) applies for the manufacturing approach of which materials in the form of powders are blended, compacted and heated to consolidate them into high-density parts. The process is widely used and allows the limitation of the post-consolidation with a little amount of waste for applications where high precision tolerances are required. The necessary steps of the powder metallurgy process are summarised in Figure 4. The elemental or alloy powder is blended with additives including (e.g. binders and lubricants) before being compacted under the required pressures where the powder surface irregularities interlock in the form of cold welding and result in a high green density. The temperature is then increased to eliminate all traces of additives and generate diffusion processes at the surface and volume of the particles to fuse the consolidate the powder and eliminate the porosity. Different process steps can be involved depending on the applications and technologies. Recent advances in powder metallurgy allow the production of parts with full densities using pre-sintering steps through high pressures compactions [24].

In contrast to conventional PM technology, additive manufacturing (AM) was developed as a transition mean from analogue to digital manufacturing process by layer upon layer material deposition. Additive manufacturing allows replicating the 3D computer model and the production of complicated 3D shapes with minimum material use and waste.

Both conventional PM and AM approaches create an advantageous trifecta of energy and material use, simplified production and complex geometries. While the powder is consolidated in the PM technology through the atomic diffusion to eliminate the porosity, powder in the AM process is consolidated through the melting and solidification of the heated material (see Figure 4).

Figure 4: Powder metallurgy and additive manufacturing process steps, modified from ASTM 2015.

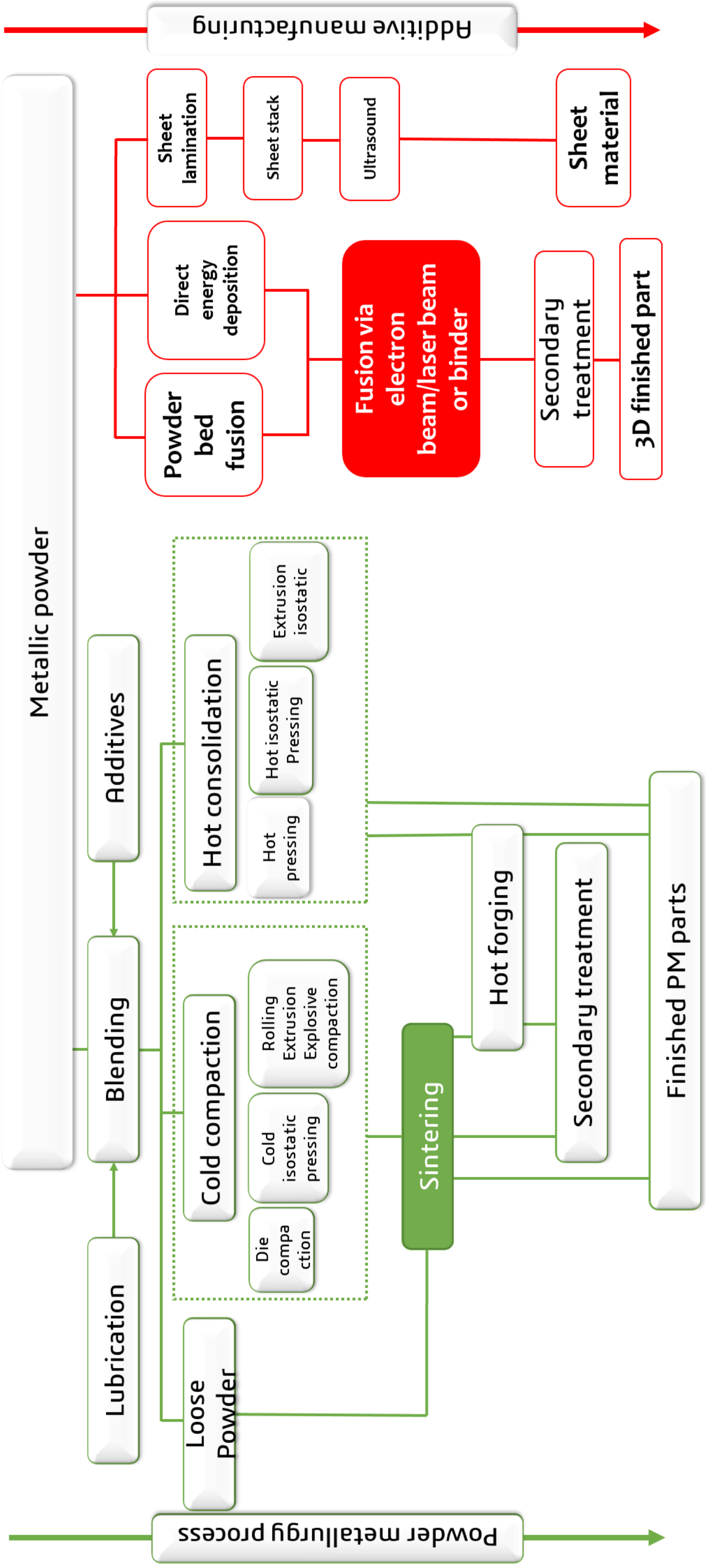

2.1.1 Sintering

Sintering is defined as the collective result of thermally activated atomic level processes through diffusion, creep, plastic and viscous flow and evaporation [25]. It allows significant strengthening by metallurgical bonding which produce the growth of contacts between particles and their coalescence. The fundamental driving force for sintering is the surface area, curvature gradients and interface energies through. The process takes place via irreversible thermodynamics events to reduce the excess surface energy through mass transport.

Different models have been proposed to define the basic parameters governing the process of sintering. Based on conventional sintering theories that identify the driving force for the sintering of powder on the reduction of the surface energy, the sintering model of free particles can be built on the following expression:

$$\sigma = \gamma . [\frac{1}{R_1} - \frac{1}{R_2}]$$

σ: driving force
γ: material surface energy
R1 and R2: principal radii of curvature and can be function of concave or convex surfaces

While initial studies were based on the discrete nature of the particles, recent effort suggested sintering kinetic also being directly linked to macroscopic factors. The continuum model includes not only sintering kinetic factors related to the properties of the particles, but externally applied forces, kinematic constraints and inhomogeneity of properties in the volume [26].

2.1.2 Sintering types

Different types of sintering can be distinguished based on the sintering materials and processes, and it includes [27]:

- Solid-state sintering: microstructural changes of the particles occur by diffusion of atoms in the solid-state. The compacted powder is usually heated to 0.5 – 0.9 of its melting point and held for a sufficient time to reach the desired density depending on the volume of the part and the properties of the materials. Solid-states sintering can be applied for both homogenous and heterogeneous materials. In the former, the neck formation and growth are a function of the competing diffusion mechanisms summarised in Table 1 and schematised in Figure 5. In the latter, alloys are formed at the contact point between particles (i.e. necks), and the further growth of the neck becomes directly depending on the nature of the alloy and rate of the alloy formation [28].

Table 1: transport mechanisms during solid-state sintering

	Material transport mechanism	*Material source*	*Material sink*
Non-densifying mechanisms: microstructural changes	1-Surface diffusion 2-Lattice diffusion 3-Gas phase transport	Grain surface Grain surface Grain surface	Neck Neck Neck
Densifying mechanisms: Displace material from grain boundary regions	4-Grain boundary diffusion 5-Lattice diffusion 6-Plastic flow	Grain boundary Grain boundary Bulk grain	Neck Neck Neck

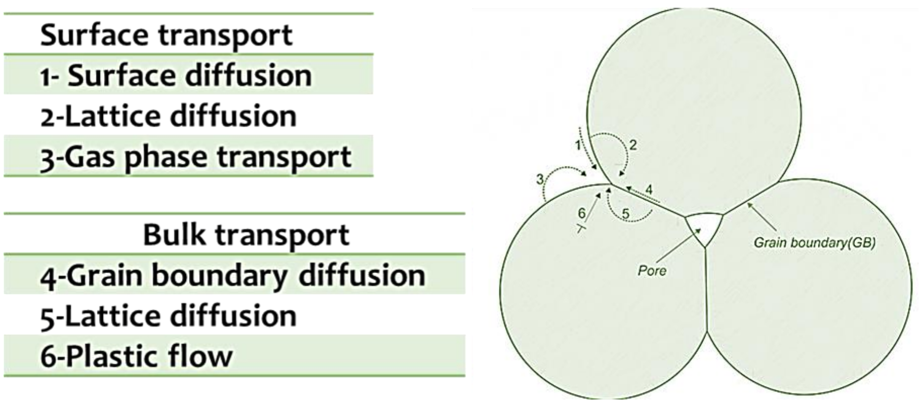

Figure 5: Diffusion mechanism during solid-state sintering, modified from [28].

- Viscous sintering: it applies to densification and deformation mechanisms in amorphous and glass material. In such material, the sintering occurs in the absence of grain boundaries diffusion mechanisms and grain growth.

- Liquid phase sintering: it refers to sintering mechanism involving the presence of a small amount of liquid phase (typically less than 20 vol%) through the addition of a metal or alloy that melts at the corresponding sintering temperatures. The high-diffusivity path for transport of matter within the liquid phase helps to achieve densification at a much lower temperature than the required temperature for the matrix. The process of liquid phase sintering is schematised in Figure 6. The liquid phase sintering occurs in three different steps through the primary and secondary particle rearrangement, intermediate solution/precipitation and solid-state sintering. At the initial stage and while the viscosity of the system is still low, the capillary pressures result in the rearrangement of the particles. The liquid phase flows around the particles grain and diffuses around the particles. Densification and coarsening happen during the second step that is dominated by solution-precipitation. Three different mechanisms are responsible for the particles coarsening: Solid-state grain boundary migration, liquid-film migration (directional grain growth) and solution precipitation.

- Pressure-assisted sintering: while the three different sintering mechanisms mentioned above do not achieve full density, the application of external pressure was found to improve the high density of the PM parts and reach full density such in the case of hot isostatic pressing (HIP), sinter forging, Spark plasma sintering and pulsed electric current sintering.

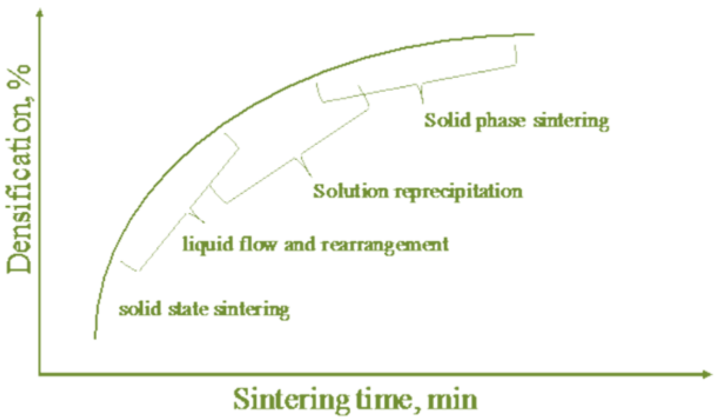

Figure 6: different densification steps during liquid phase sintering [24].

2.2 Multi-elements alloyed nanoparticles

The ability to alloy different elements into a homogeneous solid-solution structure is critical for continuous property tuning and materials development. The latter concept extends greatly the possibility to mix different elements and results in a vast panoply of properties. The fundamental challenge of creating materials mixtures and alloys is rooted to the limited immiscibility of the materials as a result of their Dissimilarities (i.e. different atomic size, electronegativity, crystalline structure, electronic structure, etc). In the bulk material, a wide range of equilibrium and non-equilibrium alloys and composition have been developed, while experimental work on nano-alloys is considered rare. Many of thermodynamic parameters such as Gibbs energy, the specific enthalpy and entropy are crystal size-dependant as the chemical potential is related to the number of atoms in the system [29]. Studies on the melting and solidification of nanoparticles revealed a modification in the solubility of chemical elements and a shift of the equilibrium curves at the phase diagram downwards towards low temperatures [30]–[32].

Due to the difficult task of analysing the chemical composition of multielement nanoparticles, many alloyed nanometric materials have been studied through the development of models to take into consideration the additional surface tension-dependant Gibbs free energy with additional segregation energy. The melting temperatures depression were found to nonlinearly decrease with increasing Cu copper concentration in for Pd–Cu systems and Pd in both Pd–Pt and Pd–Rh binary nanoparticles [33].

2.2.1 Arc discharge method

In a typical synthesis of multi-elements alloys nanoparticles, the precursors are thermally reduced or evaporated at high temperatures. In many cases, the subsequent rapid cooling process is believed to quench the nanostructure and freezes the nanoparticles into uniform alloys. Thus, the milliseconds scale thermal shock process, such in the case of the physical production method of the arc discharge and laser pulsed technologies, enables the physical, non-equilibrium synthesis of alloyed nanoparticles beyond the solubility limits.

The production of nanoparticles can be divided into three main categories:

(i) sol-gel and chemical wet methods for precipitation of oxides mainly from salt solutions

(ii) flame and spray pyrolysis of both oxide and non-oxide powders, using inorganic solutions

(iii) physical vapor techniques for nanopowder

While the chemical approaches offer better control over the size and morphology of the produced nanoparticles, the physical methods provide the possibility to scale up the production and create equilibrium and non-equilibrium phases not even possible at the microscopic bulk scale. Arc discharge allows the generation of a local high-temperature spot during microsecond. Depending on the control over the temperatures and the external parameters, condensation occurs quickly and lead to the formation of nanoparticles. This technique involves establishing a current between two electrodes.

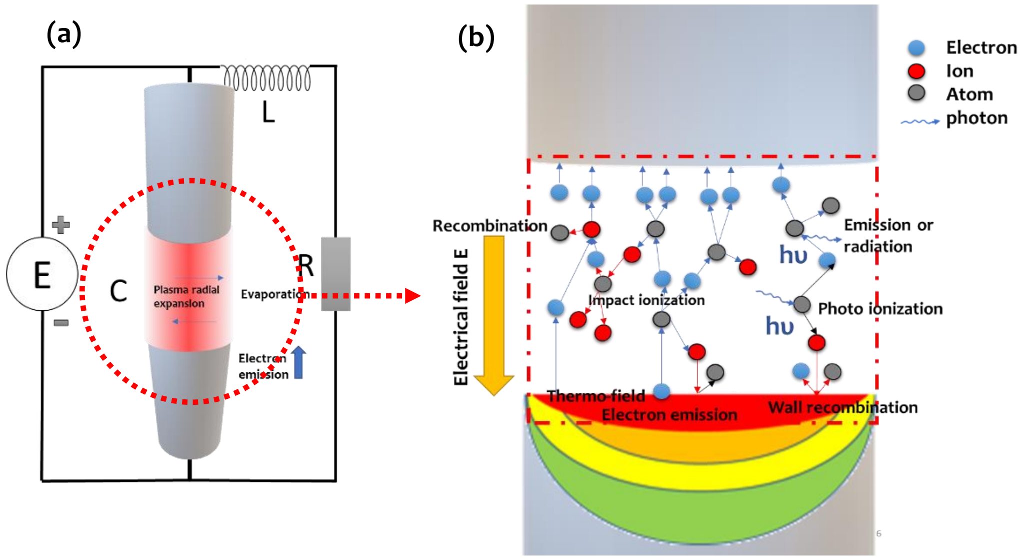

Figure 7: (a) Schematic of the arc discharge process and its equivalent electrical circuit with the two electrodes active as a capacitor, (b) main events during the spark discharge in the plasma area including ionization, electron attachment, radiation etc modified from [34].

Many variables, such as the temperature of the medium, the composition of the fluid around electrodes influence the size and the structure of the nanoparticles. In the arc discharges process, the electron flow is due to thermionic or field emission and results in an increase of thousands of degrees in the local temperature. The electrons are accelerated in the electrical field and interact with the medium present in the anode and the medium within the chamber. All kinds of matter interactions are considered in the plasma channel that gives rise to an avalanche of conductive stream composed of electrons and ions during the voltage breakdown [34]. Figure 7.a and 7.b schematise equivalent electrical circuit and the different matter interaction during the arc discharge.

An attempt to develop multi-elements low carbon steel nanoparticles through arc discharge process is presented herein. Low carbon steel rods were used as electrodes and the morphological characterisation of the powder is can be seen in Figure 8.a. The powder was found to have a spherical shape in result to the rapid and homogenous cooling in the chamber. The dark contrasts on the surface of the particles is assumed to be segregated carbon islands. Nanoparticles tracing analysis (NTA) was used to estimate the size distribution of the nanopowder. The result is shown in Figure 8.b. A large fraction of the analysed nanoparticles were found to be around 60nm size. Agglomerated nanoparticles were detected with cluster sizes above 100nm. Due to the limitation of the NTA measurement, no particles smaller than 50nm was detected. A complementary measurement using SPM technique served to map the surface of the samples (see Figure 8.c) and confirmed the presence of particles with dimensions down to a few nanometres. These particles are shown through the profiles of the three lines along the surface of the sample in Figure 8.d.

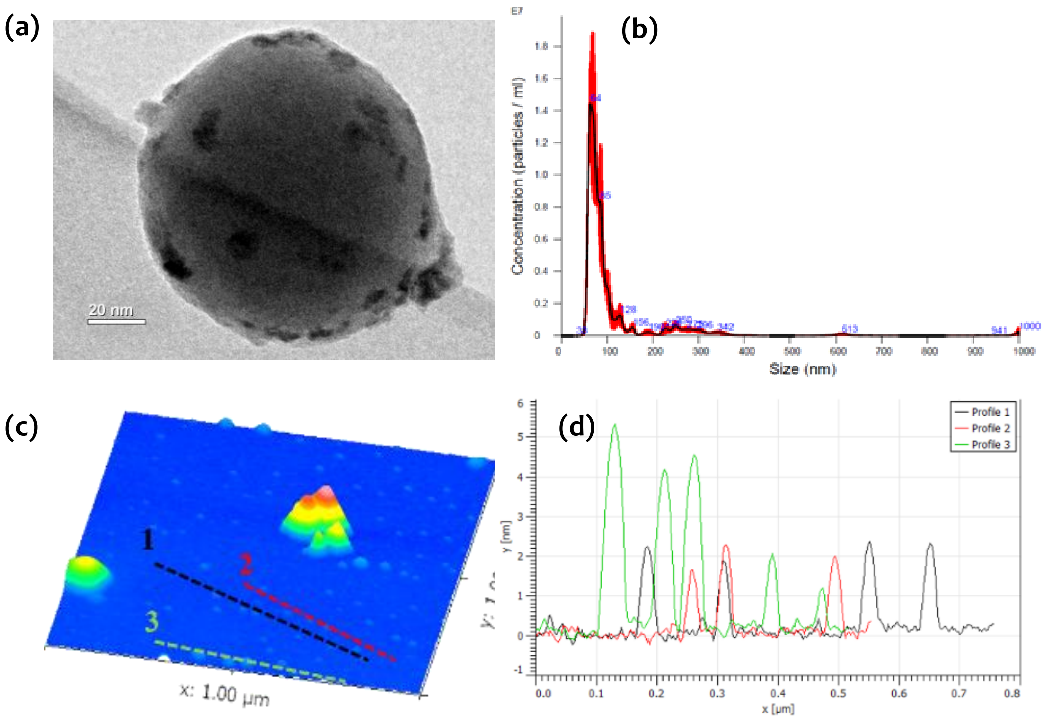

Figure 8: nanopowder morphology characterisation with(a) TEM observation of a spherical Fe NP, dark contrast on the surface of the particle is assumed to be carbon segregation, (b) Size distribution of the nanopowder indicating a mean size of 64nm, aggregated particles can be observed with peaks up to 350nm, (c) SPM mapping of nanopowder deposited on Si wafer showing the presence of particles as low as few nm.

The chemical composition of the powder was initially analysed using X-ray diffraction (see Figure 9.a). A large fraction of the powder was identified as an alpha-iron phase with peaks at 44°, 65° and 82°. Other peaks with lower intensities were difficultly distinguished and are assumed to represent iron oxides phase that was observed under TEM in Figure 9.b. A core-shell structure was observed with different contrast indicating the presence of two structures with different densities of iron. A chemical reduction treatment was performed by adding 0.1 M ascorbic acid to the nanoparticles dispersion and heated to 70 ºC. The samples were dried in the TEM vacuum. The observation of the chemically treated nanoparticles showed only one crystal structure with an aligned structure. This indicates the that the ascorbic acid reduced the shell structure assumed to be an iron oxide coating of the particles that acts as a diffusion barrier during sintering and hinder the early activation of the densification.

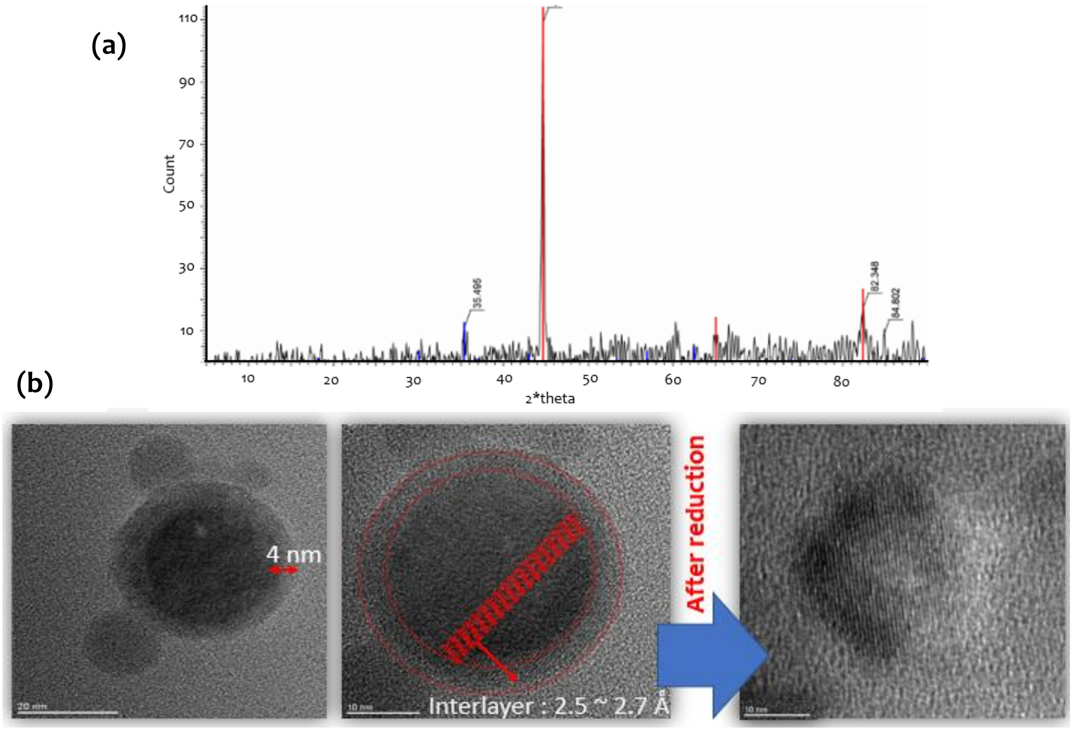

Figure 9: (a) XRD diffractogram showing peaks corresponding to alpha iron structure at 44°, 65°and 82°. Due to the low-quality signal, small peaks of iron oxide (Fe_3O_4) structure at 30º, 35º, 43º, 57º, 62° were not easily distinguished. (b) TEM observations of iron nanoparticles. A core-shell structure can be observed and is assumed to represent the iron-iron oxide structure. After chemical reduction, the particle was observed without the bright shell structure.

2.2.2 Size effect at the nanoscale

The high surface energy results in an important effect on the thermodynamic properties of the nanoparticles. The size effect is predicted to have a double consequence on reducing the melting temperature of the nanoscale object [30], [35] in addition to the densification activation and its kinetics [36].

2.2.2.1 *Melting of nanoparticles theory*

The theory of the melting depression of nanoparticles is based on the ratio between the surface and the volume of the particle [37]. The model of the melting temperature of nanoparticles can be described by combining the Gibbs-Thomson equation with the linear relationship between temperature and the particle size reciprocal [38]:

$$\Delta T_m = T_{bulk} \cdot 2\Delta. \sigma_s H_m \rho_s r_s$$

T_m and T_{bulk}: melting temperatures of the nanoparticles and the bulk materials, respectively
c: material related constant (energy and density related)
z: shape parameter (equal to 1 in the case of sphere)
r_s: radius of particle
σ_s: solid/liquid interface surface energy
ΔH_m: enthalpy of fusion
ρ_s: density of the solid phase

In the case of aggregates, the melting behaviour of the nanoscale particles was found to be affected by the number and the size of the aggregate [38], [39]. Clusters of nanoparticles form new bonds between the nanoparticles that result in reduced the surface area, lower internal energy and induce stable atomic configuration. The decrease in the surface and internal energy of the system induces a delay in the melting process of the nanomaterial and aggregated nanoparticles to show less pronounced melting depression.

In the case of the produced alloyed nanopowder, Differential Scanning Calorimetry (DSC) measurement in Figure 10 (blue curve) shows endothermic peak at 1358 ºC to indicate the melting of the nanopowder. Compared to the theorical melting of the initial bulk low carbon steel (i.e. around 1460ºC), the detected peak shows a melting depression that cannot be linked only to the size of the nanopowder. Considering the size distribution of the analysed low carbon steel nanopowder and the low heating rate during the analysis (i.e. 10 ºC/min), it is assumed that the nanoparticles sintering starts to occur before the melting takes place. In fact, since the nanoparticles are no separated and are in contact with each other, the powder form clusters of larger dimensions. It becomes important to take into consideration the clustering size and the fact that the nanosized effect is no longer conserved.

The green curve shows the change in the mass of the sample during the Thermogravimetric analysis (TGA). A three-step weight loss is observed. A decrease in the weight of the sample is seen at a temperature around 100 ºC that is assumed to be the result of the adsorption of water vapor on the surface of the powder. A second weight loss is recorded before 150 ºC and is considered the beginning of the oxide reductions that lasts until 280 ºC. A third weight loss takes places at around 500 ºC. 12.27% of weight loss is measured at the end of analysis as a result of the oxide reduction taking place at different temperatures.

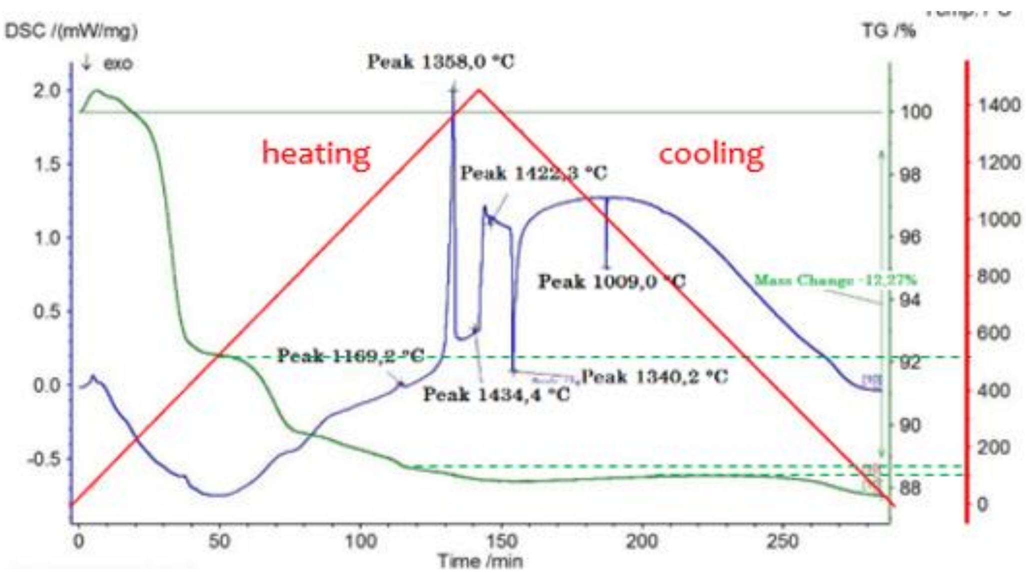

Figure 10: DSC measurement of low carbon steel nanopowder under Ar-5%H_2 atmosphere and 10 °C/min heating rate (blue curve). TGA analysis following the weight evolution during the heating of the low carbon steel nanopowder (green curve).

2.2.2.2 *Sintering of nanoparticles*

In addition to the morphology of the particle, the sintering process is directly affected by the size of the particle and concomitant the microstructural properties from the catalytic effect to the mechanical and the physical properties. Despite the melting process of the nanoparticles above a certain threshold is not apparent, the sintering kinetic of nanoparticles can still show important dynamic as a result of the high surface energy of the particles. Nanoparticles sintering occurs rapidly due to shorter diffusion distances and higher contact pressure.

The sintering kinetic of the nanoparticles as a function of the temperature can be expressed by the following model expression [40]:

$$\ln\left(\frac{D_2}{D_1}\right) = \frac{Q}{3R} \cdot \left[\frac{1}{T_1} - \frac{1}{T_2}\right]$$

T_1 and T_2: sintering temperatures of the particles of dimensions D1 and D2, respectively
Q: Activation energy for the predominant mechanism
R. gas constant

The result of the dilatometry analysis is presented in Figure 11. A linear expansion at the beginning of the heating is observed as a result of the thermal expansion coefficient of the iron powder. At temperatures around 100 °C, a shrinkage starts and continue until the temperature reaches the maximum of 930 °C. The latter shrinkage indicates an early reduction of the oxides and agrees with the results obtained from the DSC analysis. It also indicates the densification of the powder through an early activation at temperatures relatively low. At temperatures of 502.42 ºC, 685.74 ºC, 759.46 ºC and 857.42 ºC, the slop of the curve changes considerably in the heating step as a sign for different structural expansions and contractions (i.e. red curve).

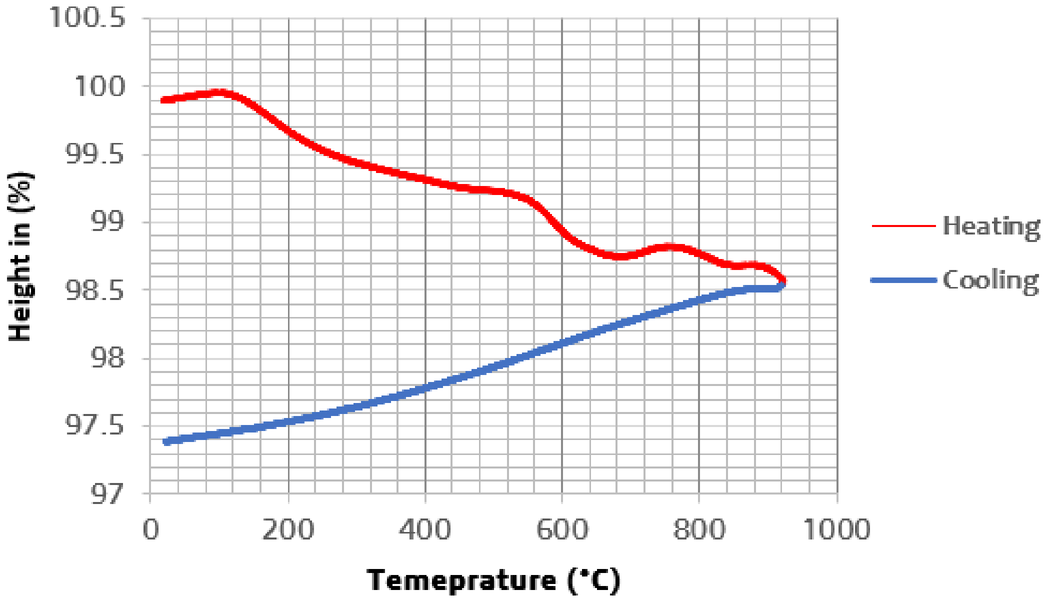

Figure 11: Dilatometry analysis of the produced alloyed nanopowder at temperature gradient of 5 ºC/min and under argon atmosphere.

The explanation of such behaviour is not clear, but since the latter events are no longer visible in the cooling step where the slop of the curve is seen almost constant (i.e. blue part), it is assumed that solubility-size -sintering kinetic play an important role in such result. The rapid densification process in the case of nanoparticles is known to result in an early isolation of the pores that might delays further oxides reduction and shrinkage. This can be observed in the TGA curve at the temperatures prior to 500 ºC where the rate of weight loss is reduced. Once the temperature goes above 500 ºC, the third step of the weight loss starts and is accompanied with a further shrinkage observed at 502 ºC in Figure 11. Besides, as discussed earlier, the phase diagram of alloyed nanoparticles is shifted towards lower temperatures comparatively to the bulk equilibrium phase diagram with allotropic phase transformation of phase into gamma-austenite iron phases and verse versa. An additional factor to consider in this conditions is linked to the sintering induced phase change [41]. Since the cooling step does not show any obvious expansion/contraction, it is assumed that no phase change occurred during the cooling. This indicate that the equilibrium phase at room temperature is the same as the one at 930 ºC and is alpha-ferrite iron phase. Thermal events between 500 ºC and 930 ºC require further investigation.

Previous work on the densification of plasma discharge-produced iron nanopowder with oxide layer on the surface reported a sintering mechanism starting at 270 ºC in the under argon/H_2 atmosphere [42]. In the case of dilatometry analysis of the produced alloyed nanoparticle, no reducing agent was used during the dilatometry analysis performed under argon atmosphere. The result presented here indicates the early activation of the densification after the reduction of the oxide using the carbon content within the powder as a self-reduction process. This work shows that the composition of the particles plays a novel effect for the self-reduction of the oxide layer. Such approach indicates that the low carbon steel nanoparticles not only can be used as a sintering aid in PM technologies, but also as a promising approach for cost efficient process that limits the use of additives for the reduction of the oxides during the sintering process.

Chapter 3: Graphene for thermal dissipation in electronics

3.1 Introduction

Carbon materials have attracted increasing interest due to their outstanding performances combining physical, mechanical and chemical properties. Carbon materials family includes a verity of zero-, one-, two-, and three-dimensional allotropes as in fullerene, carbon nanotube (CNTs), graphene, diamond and graphite, respectively [43]. All the different dimensionality of carbon allotropes can be found in the schematic representation in Figure 12. More importantly, the 2-dimensional graphene structure emerged as a material for the future of nanotechnology with outstanding properties and will be the subject for the focus of this thesis.

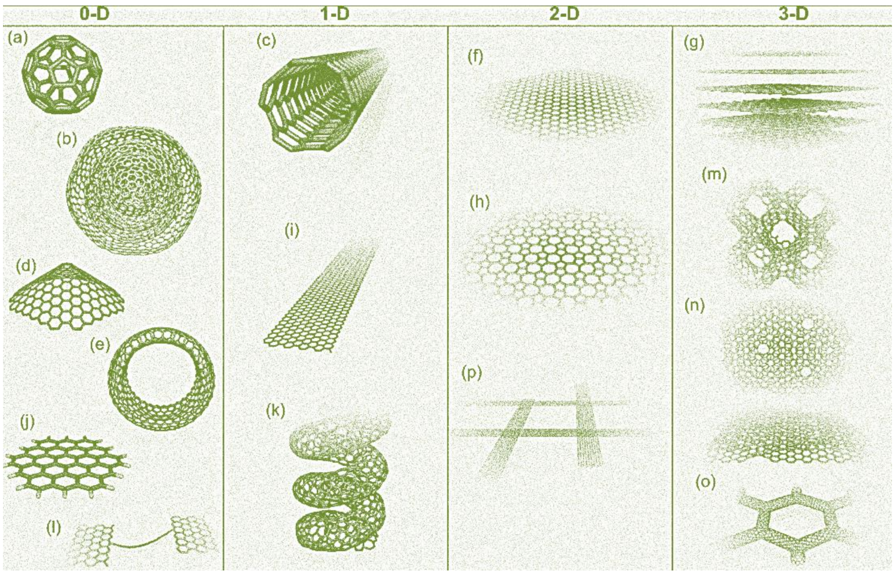

Figure 12: Carbon allotropes with sp2-like hybridized carbon nanostructures (a) C60: Buckminsterfullerene; (b) nested giant fullerenes or graphitic onions; (c) carbon nanotube; (d) nanocones; (e) nanotoroids; (f) graphene; (g) 3D graphite ; (h) Haeckelite surface; (i) graphene nanoribbons; (j) graphene clusters; k helicoidal carbon nanotube; (l) short carbon chains; (m) 3D Schwarzite crystals; (n) carbon nanofoams (interconnected graphene surfaces with channels); (o) 3D nanotube networks, and p nanoribbons 2D networks. Reproduced from [42].

3.1.1 Properties of graphene

Identified in 2004, graphene is a metastable form of carbon with sp^2 hybridisation in a honeycomb lattice, with a thickness of few atomic layers and less than 1000 atoms/nm. It is 100 times stronger than steel, flexible as an elastic polymer, with high field emitter properties and superior electrical and thermal conductivity.

Graphene can be found as monolayers or multilayers structures with a number of layers, their stacking mode and composition dictating its properties [44]. Even though considered as a 2D structure, graphene properties emerge from the 3D electronic cloud around the layer [45].

Figure 13 shows the energy band structure in the case of single-layer graphene. Graphene is a zero-band gap semi-conductor where single-layer graphene mimics a system of relativistic Dirac particles with zero rest mass. When the number of the layer is increased, the graphene electronic properties turn to a semi-metal. In the two layers system, the region around the *k* shows a minimal anti-crossing overlap of 1.6 meV toward the T point due to the interaction between B and B' atoms of carbon as a semi-metal, while displaying a crossing behaviour when moving away from the T_K region in the Brillouin zone. Above three layers, the graphene systems can be described as semi-metallic in which the B carbon atom interacts with the next-nearest -neighbour planes. The increase in the band overlap increases further with the increase in the number of graphene layers. Finally, at a number of layers above eleven, the difference in the band overlap becomes less than 10%, and minor modifications are observed [46] .

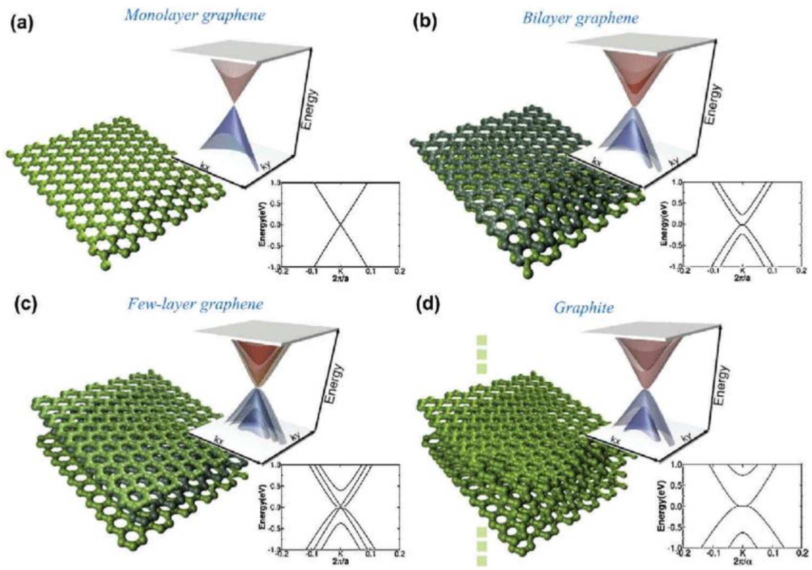

Figure 13: Low energy DFT 3D band structure and its projection on k_x component close to K point for (a) monolayer graphene, (b) bilayer graphene, (c) trilayer graphene and (d) bulk graphite.

Multilayer graphite can fellow different stacking structures that affect its properties. Graphene stacking can be identified in a Bernal stacking as the thermodynamically stable form or Rhombohedral stacking that is metastable and is known to coexist in bulk graphite at volume fractions that vary significantly with the production process (see Figure 14). The difference in the stacking structure result in a difference in the distinct structural symmetries of which Bernal stacking is non-centrosymmetric and the latter is centrosymmetric [47]. While the single-layer and bilayer graphene are considered semimetal, the few layers graphene would be either semi-metallic or semi-conductor in the cases of Bernal or rhombohedral, respectively [24]. In Bernal stacking, half of the carbon atoms from the second layer coincide with the carbon atoms of the first layer, while the other half lies above the centre of the hexagonal lattice of the first layer in an ABA stacking. An angle of 0-30° can be found in twisted multilayer graphene as in AA' stacking, and a magical angle of 1.1° led the discovery of unconventional superconductivity in graphene [25]. Rarely all the atoms match the positions of the carbon below with a 0-angle -stacking structure and layers can be shifted as an ABC stacking is rhombohedral structure.

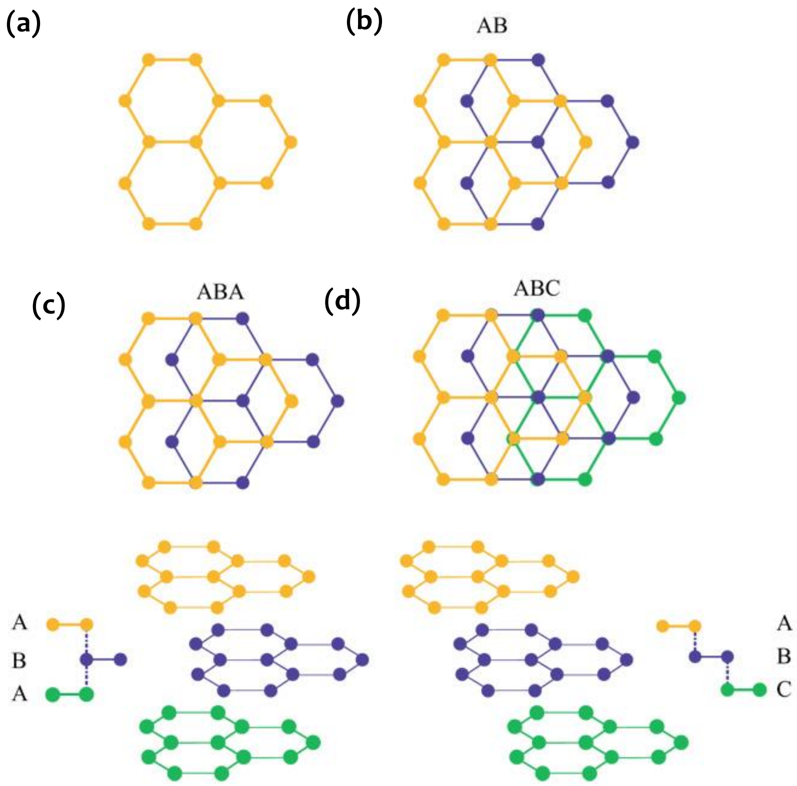

Figure 14: Different stacking sequences on the base of (a) Graphene monolayer and (b) AB-stacked graphene bilayer resulting in (c) ABA (Bernal stacking) and (d) ABC (rhombohedral stacking), adopted from [46].

3.1.2 Graphene-metal interaction

One important aspect of the interest developed for graphene is the graphene/metal interaction that plays a major role in the chemistry and physics of the graphene/metal interface and the properties. Substrate-induced effects are a critical aspect of graphene material science that results in various properties. The arrangement of the substrate atoms with the carbon atoms strongly affects the bonding between the graphene and the metallic substrate and results in different interface separation and binding energy [48]. Four different structural arrangements of graphene/metallic substrate with a direct effect on the graphene properties to either form metal carbide and lattice mismatch (see Figure 15) [47]. Through to the competition between carbon–carbon and carbon–metal interactions, the carbon-metal can be classified as [50]:

- Weak interaction in the case of silver, gold, copper and platinum substrates, and is formed where the carbon atoms are located on the triangular hollow sites of the metallic substrate.
- Strong interaction in the case ruthenium, platinum, rhodium, and iridium substrates and can occur as a result to (i) formation of carbides during the deposition (ii) small graphene/substrate separations where the substrate lattice and the graphene lattice match well,(iii) a substantial alteration of the graphene π-band, in particular, a shift to the higher binding energy of 1–3 eV and opening of a bandgap; and (iv) large corrugation of the graphene layer with buckling of more than 1 Å is observed.;
- Very strong carbon metal interaction where the carbon atom intercalates the layer of the substrate in the case of palladium substrate.

The presence of the metallic structure at the proximity of the graphene induced a doping effect on the graphene that was reported with graphene on Ag and Cu as n-type while p-type doping in the case of Pt was measured with the Dirac point 0.3 eV above the Fermi level [51].

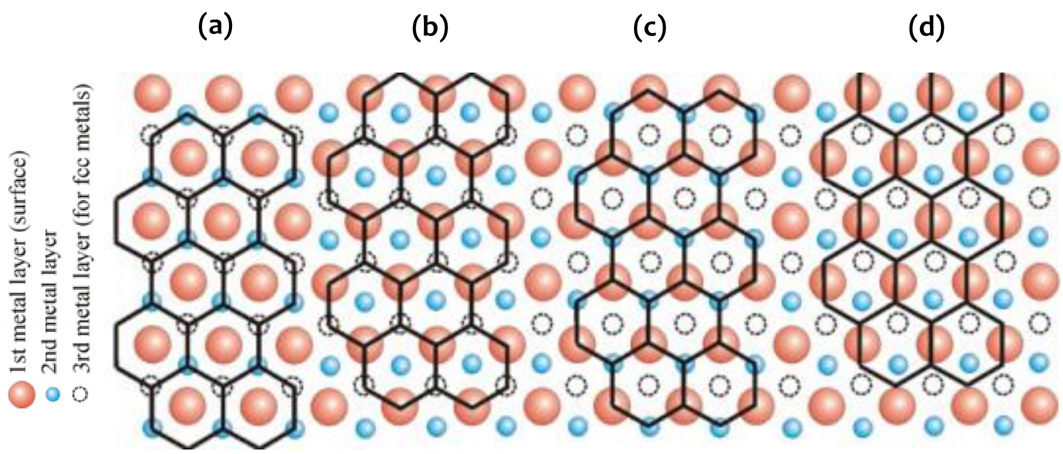

Figure 15: the different four low symmetry adsorption configuration of (a) graphene atoms are located in three-fold hollow sites of the surface, (b) carbon atoms are alternately occupying metal-atop sites and the 'FCC' hollow sites, (c) carbon atoms are alternately occupying metal atop sites and the 'HCP' hollow sites, (d) adsorption structure in the case of bridge [49].

3.1.3 Synthesis of graphene

Current development in material science has led to more controllable approaches for the growth of graphene. Two main growth mechanisms can be listed [52]:

- Precipitated growth: in the case of strong interactions carbon-metal such in the case of nickel. First, the carbon atoms dissolve into the catalyst at high temperatures. During the cooling step, the solubility of the substrate in carbon is decreased and the carbon atoms segregates at the surface in the form of multi-layer graphene.
- Diffusive growth: in the case of weak interactions carbon-metal such in the case of copper and silver, the decomposed carbon atoms stay at the surface and diffuse in a rate that dictates the nucleation and growth of monolayers graphene grains. The table below lists some of the methods used commonly to produce single or multilayers graphene:

Table 2: Production methods for single and multilayers graphene

Single-layer graphene	Multilayers graphene
Reduction of single-layer graphene oxide	Reduction of multilayers graphene oxide
Chemical vapor deposition	Thermal exfoliation
Epitaxial growth	Aerosol pyrolysis
Micromechanical cleavage	Arc discharge
Dispersion in polar solvent	

3.2 Nanofluids

The electronics devices with heat fluxes over 1000 W/cm^2 require the use of advanced thermal dissipation technologies such as liquid cooling. For examples, single-phase liquid cooling technologies as the microchannel heat sink, and two-phase liquid-cooling technologies as heat pipes and thermosyphons are currently used in the industry. However, due to the inherently low thermal conductivity of the fluids, nanoparticles with an average size below 100 nm were introduced as fillers suspended in fluids. The approach was found to have a positive effect on the thermal properties of the base fluids. Reports on nanoparticles dispersed in liquid fluids indicate [53]:

- large surface area for heat transfer, with a large number of electrons available on the surface;
- Enhanced convection as a result of the low particle momentum and very high mobility;

- Nonlinear relationship between the concentration of the nanoparticles within the fluid and the thermal conductivity enhancement and strong dependence on the temperature and the size of the nanoparticles;
- increased in the laminar heat transfer coefficient is by a factor of up to 3.5 while the natural convection heat transfer coefficient is negatively affected by the presence of the nanoparticles;
- Significant enhancement in the turbulent heat transfer coefficient.

3.2.1 Graphene coated nanoparticles as additive for water-based fluid

In this work, graphene-coated copper nanoparticles were developed in collaboration with SHT Smart High-Tech AB, Sweden using the top-down physical route of arc discharge.

The graphene coated copper nanoparticles were observed under TEM and found to exhibit a spheroidal to spherical morphology (see Figure 16.a). The coating was observed to surround the particles with a varying number up to fifteen layers. The SPM analysis in Figure 16.b shows a size distribution with an average size of 57.5nm and a maximum of 87.27nm.

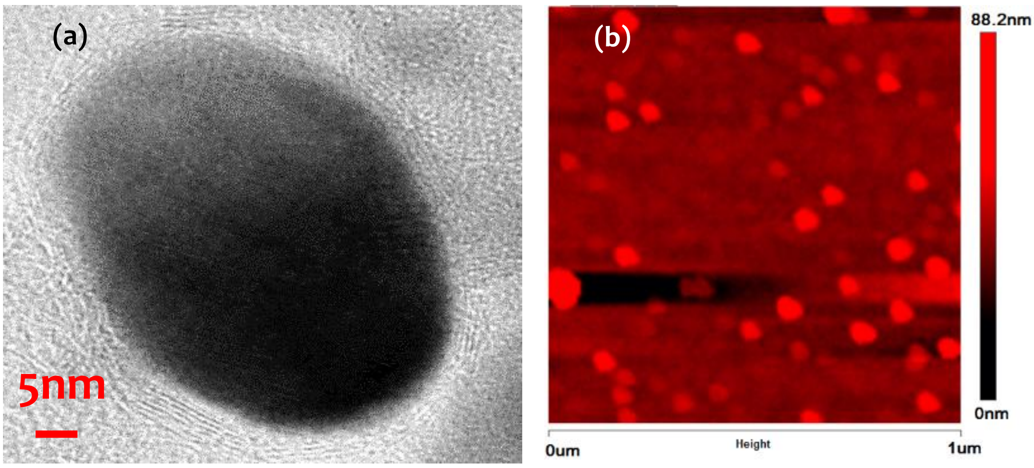

Figure 16: (a) TEM observation of copper coated nanoparticle. The graphene coating can be seen embedding the particles. (b) SPM result of the copper nanoparticles shwoing a size distribution up to 88.2nm

XPS analysis was used as a surface analysis method in order to investigate the origin of the coating. The result is shown in Figure 17 with the deconvolution of the C1s into three primary and one minor component. The main peak and their identification are summarized in table 3.

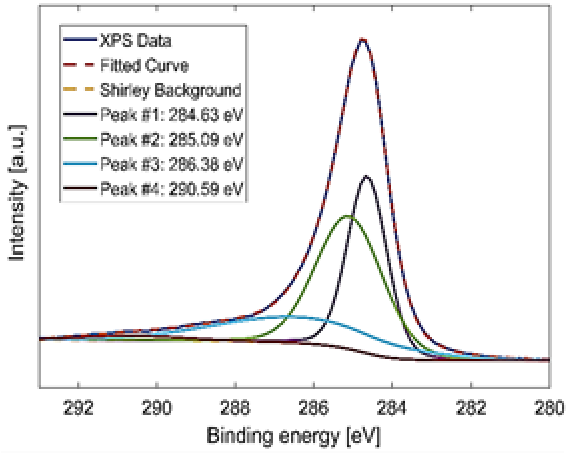

Figure 17: Deconvolution of the C1s peak from XPS analysis. Three main peaks are created in addition to a minor peak

The result of the of the XPS analysis confirm the nature of the graphitic structure the carbon layers around the copper nanoparticles. The sp2 bonds of carbon constitute the basic nature of the 2D graphene while the sp3 bond indicate the presence of multilayer configuration. The presence of oxygen bonds can be due to the impurity formed during the handling of the sample.

Table 3: XPS peak deconvolution of the carbon peak

Peaks position (eV)	Identification
284.63	sp^2 carbon, main lattice
285.09	sp^3 carbon, amorphous carbon/defects
286.38	C-O-C bond
290.59	C1s satellite

Zeta potential results of the dispersed nanofillers in water are shown in Figure 18 with an average value of 6.22mV. With such low value, the dispersion is not stable, and the particles are prompt to aggregation.

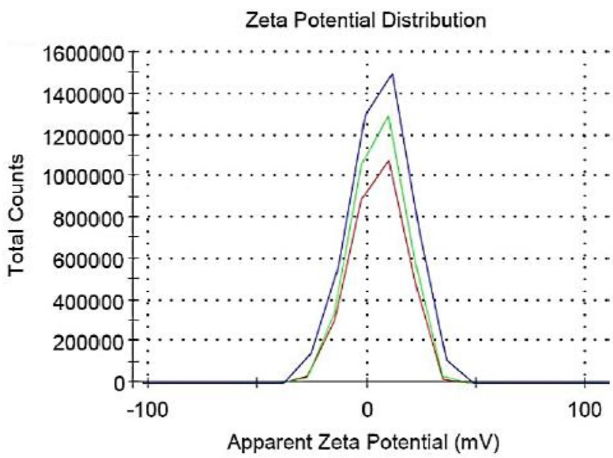

Figure 18: Zeta potential measurement of three samples of graphene coated copper nanoparticles

3.2.2 Thermal conductivity and viscosity of the nanofluid

Many theories have been developed in order to explain the correlation between the thermal conductivity variation and the presence of the dispersed nanoparticles. Studies have suggested the increase of thermal conductivity in nanofluids can be explained by [54]:

i. Increase in thermal transfer due to nanoparticles free motion (i.e. Brownian motion);
ii. Nanoconvection in the fluid;
iii. Agglomeration of nanoparticles;
iv. increased interatomic interactions that lead to an increase in thermal energy transfer;
v. Layer-like ordered liquid molecules around the solid;
vi. Ballistic phonon transport of heat through solid nanoparticles.

The thermal conductivity of graphene coated copper nanoparticles in water were evaluated at temperatures varying from 25 to 45 °C and with concentrations of 0.1w.%, 0.05 w.%, 0.02 w% and 0.01 w.%. The fluids were sonicated under 2W for 10min to disperse the particles. No surfactant was used in this initial work. Figure 19 shows the result of the thermal conductivity of nanofluid using the hot disk method. The thermal conductivity for the different samples was found to vary linearly with the variation of the temperature and the concentration. A positive correlation can be seen as the temperature increased while the most significant improvement was registered for the highest concentration and at a temperature of 45 °C.

As the graphene coated nanoparticles copper nanoparticles were found to have a small stability in the solution, the effect of the fluid molecules is not considered. It is assumed that the presence of the nanofiller within the solution increased the thermal conductivity of the fluid through the contribution of the solid phase conduction. As the concentration increased, the contribution of the conduction in the thermal transport also increased. The improvement in the thermal conductivity of the nanofluid as the temperature increased is assumed to be due to the variation in the nanoconvection and the Brownian motion that is directly related to the temperature of the fluid.

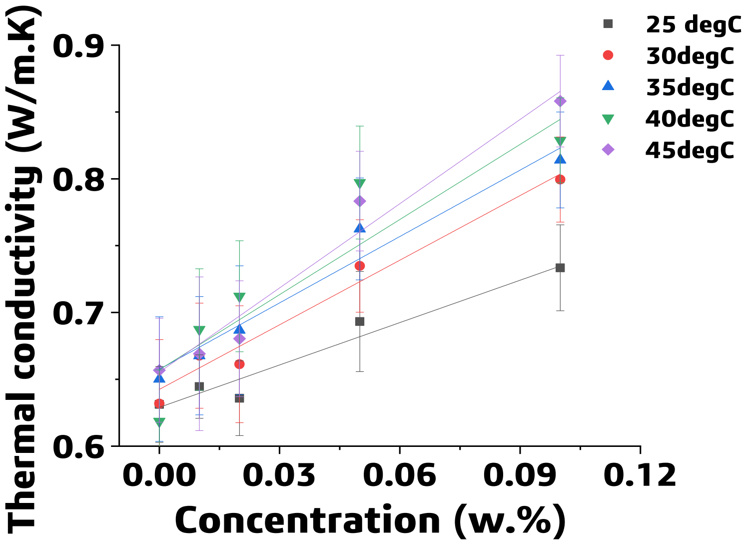

Figure 19: Thermal conductivity measurements of the different concentration of NFs at temperature of 25°C, 30°C, 35°C, 40°C and 45°C.

Figure 20 shows the results of measurement of the viscosity of the different concentrations of the nanofluids. Water viscosity is measured as a reference. The results confirm the nature of the Newtonian behaviour of water where its viscosity remains relatively unchanged with the applied shear rates. The increase in the concentration of the nanoparticles in the fluid increased the viscosity of the fluids. However, the presence of the nanofillers did not show a difference in the rheological properties of the fluid except for the high concentrations of 0.05 w.% and 0.1 w% at a low shear rate where the nanoparticles formed aggregates.

Graphene coated copper nanoparticles explored in this work were found to exhibit a positive effect on the thermal conductivity of the fluid. As the graphene is known to act as a protective layer against oxidation, the latter approach allows potential use of the metallic coated nanoparticles as nanofiller for liquid based cooling technologies. An additional effort should be invested in improving the stability of the nanofillers in order to ensure homogenous and reliable properties.

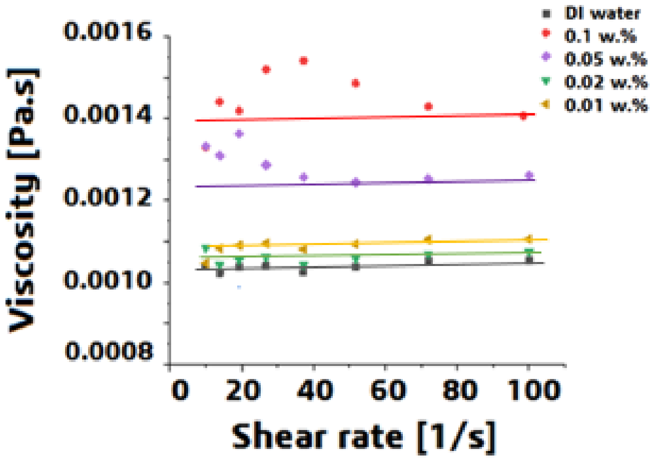

Figure 20: viscosity analysis of the copper coated NFs. The aggregation effect is seen at low shear rate and high concentrations

3.3. High porosity graphene foam for heat dissipation

An example of non-conventional material design that combines high surface area with high thermal conductivity can be found in metallic foams. While offering a good compromise between high levels heat dissipation with limited power and cost, this passive approach also combines low density and light weight, high surface area to volume and high mechanical properties. The thermal properties of these foams were found to be directly related to the intrinsic thermal conductivity of the solid phase first, but also the porosity level and the nature of the filler or the fluid flowing through it.

3.3.1 Graphene foam heat sink

3.3.1.1 From 2D to 3D graphene structures

Various production methods of the 3D graphitic structure have been proposed and can be correlated to different properties and applications. The production of 3D graphene structures methods includes a foam-like template or a aerogels/hydrogel and can be categorised into three primary strategies: direct synthesis of 3D graphene, assembly of graphene oxide sheets and template-assisted assembly. While the two latter methods result in modest structural and physical properties, the direct synthesis of the graphene foam via Chemical Vapor Deposition (CVD) is the most reliable.

CVD growth of graphene foam implies the use of pre-fabricated 3D metal substrates such as Ni foam that acts as a catalyst and template for the growth of the foam. The porous nickel foam is subjected to pyrolyzed methane gas (CH_4) at temperatures of 1000 °C and ambient pressure at constant rates. After the growth, a thin film of polymethyl methacrylate (PMMA) is coated on the graphene and used as protection from the etchant while it holds the structure before the etching using hydrochloric acid (HCl) or $FeCl_3$ solution to remove the nickel. Finally, the foam is immersed into hot acetone to remove the PMMA [55]–[57].

3.3.1.2 3D-high porosity graphene foam

In recent years, a focus was given to the 3D high porosity graphene foam. The 3D structures consisting of ultrathin graphite reached a value higher than 1500 W/mK that is 10 times higher than the thermal conductivity of aluminium for only the fifth of its density [58], [59]. While the increase in the number of layers of graphene is known to deteriorate its thermal properties and affect negatively the overall performances [60], the increase in the carbon-based structure thickness was found to result in an additional enhancement through the increase in the high thermal conductivity solid matrix fraction. For instance, the effective thermal conductivity of electroplated copper on a reticulated vitreous carbon foam reached 100% enhancement at 5% solid density increase and up to 3500% enhancement at 52% in density [61].

3.3.1.3 Phase change materials

Different forms of energy storage such as mechanical, electrical, chemical or thermal approach car used in different applications. In Electronics, the thermal energy storage includes sensible heat that and is used as energy to raise the temperature, while latent energy storage is based on the heat release or absorption during a phase change from solid to liquid to gas and verse versa. A large number of Phase Change Materials (PCMs) (organic, inorganic and eutectic) are available with a wide range of physical, kinetic, chemical and thermal properties and paraffin wax is the most promising ones for the electronics thermal management. Paraffin is largely available, reliable, not toxic and stable with little volume change and consists of chains of n-alkanes of CH_3-(CH_2)-CH_3 that involves significant amounts of heat during the phase change. However, the thermal conductivity of paraffin grades is low and different approaches are deployed to enhance their thermal properties. Nanoparticle-enhanced phase change materials have been extensively studied with different types of nanoparticles, concentrations and dispersion methods [62][63]. Despite the positive impact on the thermal properties, results showed short term stability of the mixtures as a consequence of the segregation and deposition of nanoscale fillers. In addition to offering a template to strengthen the mechanical properties of the PCM, non-movable matrix on the other hand shows promising improvement in the thermal properties.

3.3.2 High porosity graphene foam heat sinks and container for PCM

Recent developments in the heat dissipation in electronics led to the use of high thermal conductivity, high porosity and lightweight materials as composites for a mutual property enhancement. PCM plays a role in the improvement of the thermal behaviour of the foams through the enhancement of the heat transfer at the pore level and the improvement of the convection at the interface of the liquid phase with the absorbed heat [64]–[66]. In the case of copper foam/PCM system, the thermal conductivity enhancement reached 200% comparatively with pure PCM [67], and a temperature drop of up to 30% was reported in the case of aluminium foam [65], [68]. Nickel foam was also impregnated with PCM and achieved a temperature decrease of 24% [69],while the later reached an increase of 23-fold by growing graphene on its surface [70].

In this work, the PCM was infiltrated incrementally within the graphene foam/silver composite, and the temperature profile of the thermoresistor was recorded. Silver nanoparticles sintering was used to attach the graphene foam on the back surface of the heater. The high porosity material was deposited on top of the wafer and sintered at 290 °C. Additional silver nanoparticles were added and sintered under the same conditions in order to strengthen the 3D structure. Different amounts of PCM were then added, and the thermal properties were investigated and compared to graphene foam/silver coating, graphene foam and nickel foam. Figure 21 is a simplified schematic of the sample preparation steps.

SEM observations of the 3d porous structures are presented in Figure 22. The addition of the sintered silver nanoparticles can be observed Figure 22.a with a bright contrast filling the concave surface of the graphene foam with a coating of less than 500nm (see Figure 22.c) and a relatively high density after sintering (see Figure 22.d). The structure of the secondary microchannels is indicated in Figure 22.b. The attached structure of graphene is presented in Figure 22.e where the flexibility of the foam allowed to reach good quality contact without the application of external pressure. Due to the stabilization of the graphene with the ethylene glycol used as a dispersion medium for the silver nanoparticles, the contact point at the interface graphene/silver is seen through the opening of the strut in Figure 22.f.

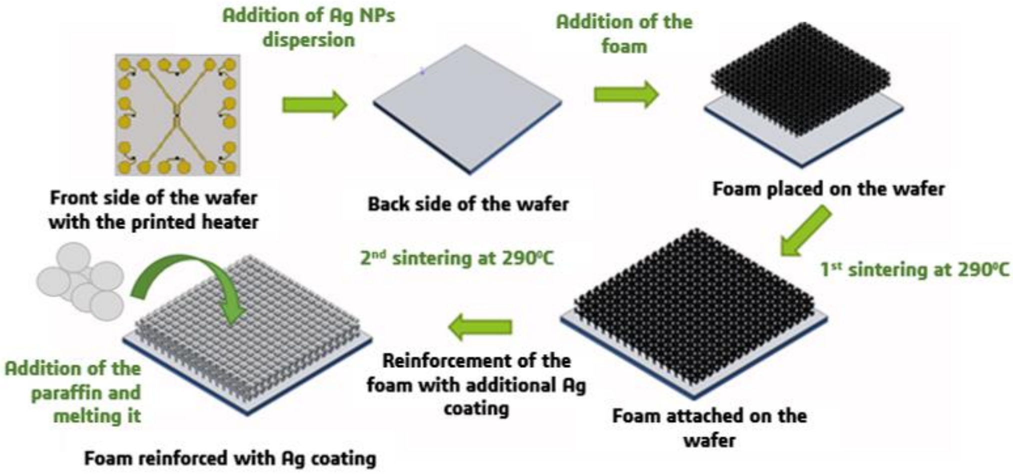

Figure 21: schematic representation of the sample preparation of graphene foam/silver composite. A layer of Ag nanoparticles is first coated on the back of the heater; the foam is then deposition and sintered. Additional Ag coating is added and sintered under the same conditions. The PCM is melted and infiltrated gradually into the porous structure.

The result of the DRT Joule heating for the thermal conductivity measurements of the porous structure of graphene before and after the addition of the silver coating are shown in Figure 23.c and 23.d, respectively. The variation of resistivity in the case of

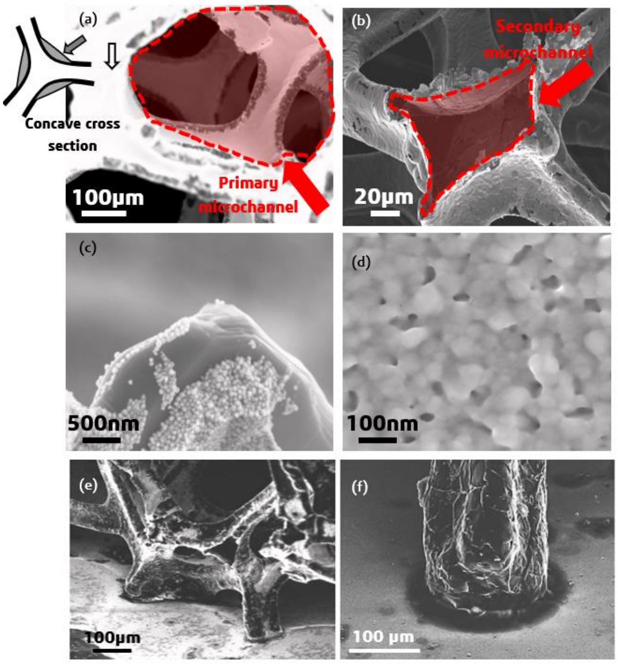

Figure 22: (a) graphene foam coated with Ag NPs, (b) Internal secondary microchannels within showed on broken foam node, (c) Ag NPs deposited on graphene sheets, (d) Sintered Ag NPs at 290ºC, (e) foam struts in contact with the substrate and (f) zoom-in at the contact of the strut/substrate.

graphene foam followed a nonlinear inverse proportional resistance increase with the current due to the negative temperature coefficient of resistance of graphene and reached a value of $1{\cdot}10^{-3}\ \Omega.m$. With a positive temperature coefficient of resistance, the presence of silver switched the mode of conduction to pure metallic behaviour with a proportional increase in the resistance with temperature as an ohmic linear behaviour with a resistivity value of 2 W/mK. Considering a solid volume fraction of 0.45 vol.%, Using the parallel composite model, the values of thermal conductivity for the graphene foam with and without silver corresponded to values of 319 W/mK and an increase to 352 W/mK when the silver coating and the porosity level changed from 99.6% to 99.44%, respectively.

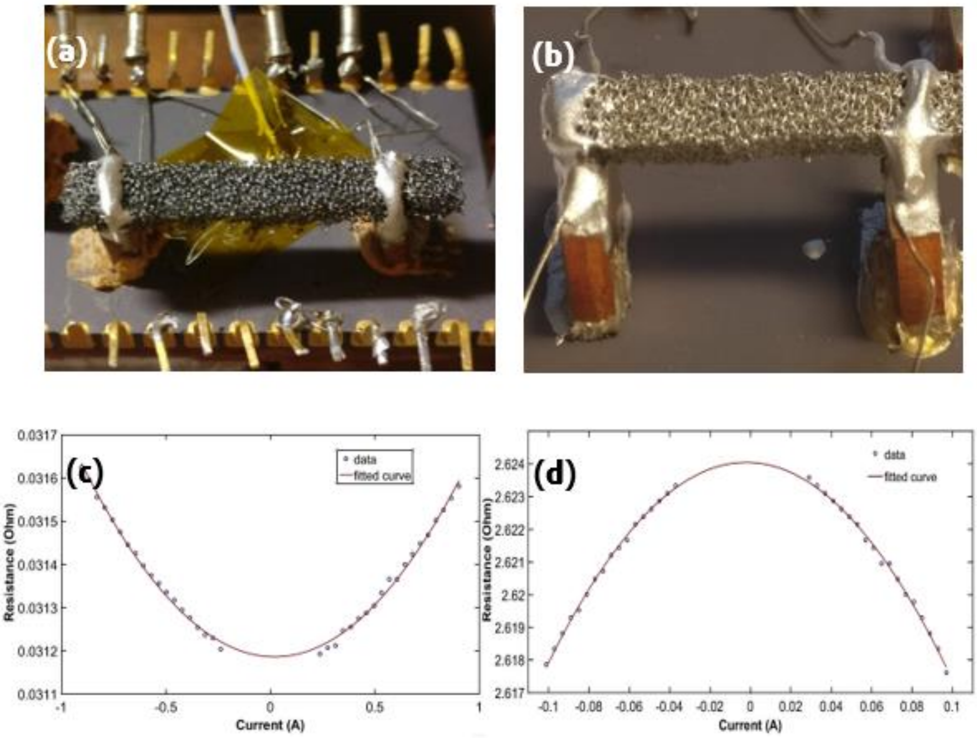

Figure 23: DRT setup and results of the measurement. (a) photograph of the graphene foam suspended between two copper blocks; (b)photograph of graphene foam coated with silver and suspended between two copper blocks; (c) Resistance measurement at different current.

3.3.2.1 Graphene foam as a heat sink and PCM container

The thermal properties of the high porosity structures were evaluated and plotted in Figure 24. The graphene foam with Ag coating was found to exhibit the best thermal behaviour comparatively to the metallic nickel foam and heater without a heat sink (see

Figure 24. a and b). Due to the higher thermal conductivity of the graphene foam/silver, the junction temperature in the case of the graphene foam/silver was the lowest at

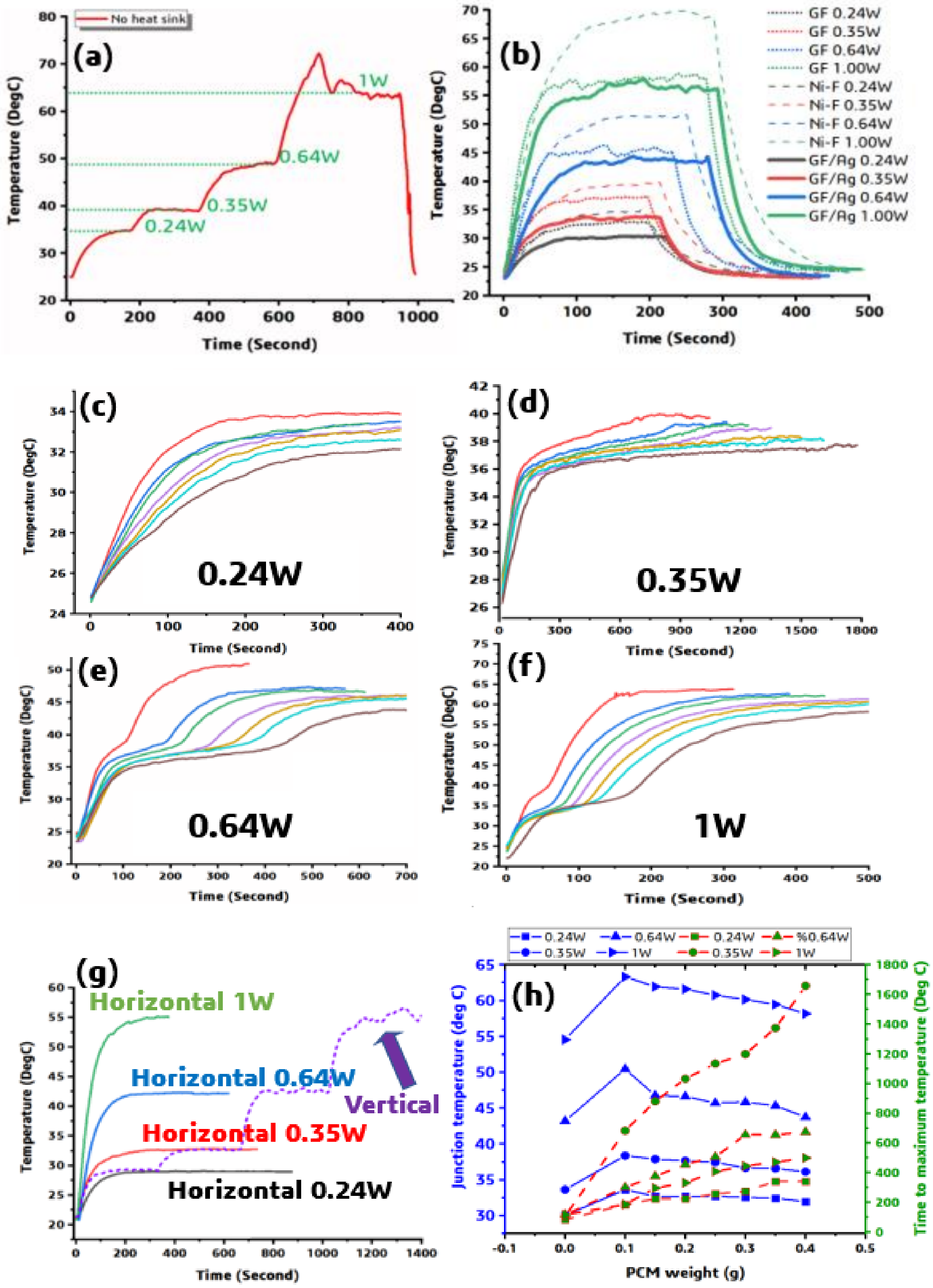

Figure 24: Temperature rise at different power level in the case of (a) no heat sink and (b) three heat sinks (i.e. graphene foam (GF), nickel foam (Ni-F) and graphene foam coated with Ag (GF/Ag). Transient temperature of graphene foam coated with Ag with different PCM load at: (c) 0.24W, (d) 0.35W, (e) 0.64W and (f) 1W. (g) Measurement comparison of graphene foam coated with Ag at horizontal and vertical orientations. (h) Summary of the junction temperatures (blue) and time to reach the maximum temperature (green/red) at different power levels and PCM loads

different power levels. At 0.24 W and 0.36 W, the junction temperatures of nickel foam were comparable to the ones of the heater without a heat sink. At higher power levels, nickel foam performed poorly comparatively to the heater and resulted in higher junction temperatures. It is was assumed that the sintered nickel foam performed poorly in a result of limited contact between the solid foam and its substrate.

Incremental amounts of paraffin were added to the graphene foam, and the evolution of the temperature of the heater was recorded in the case of GF-Ag. The high porosity foam contained the melted PCM at different levels and up to a 0.4g of paraffin before it started to drip. The results of the thermal behaviour of the graphene foam coated with sintered silver and infiltrated with paraffin are shown in Figure 24 (c-f). Higher amounts of PCM resulted in the improvement of the thermal conductivity of the GF-Ag/PCM system and lower junctions temperature. No delay in the time to reach equilibrium was observed at 0.24 W. The maximum temperatures reached during the heating step with low power were lower than the melting point of the PCM. The highest time delay achieved was in the case of 0.36 W since the heat flux generated at this power resulted in a low melting rate. The addition of PCM resulted in longer time to melt entirely and resulted in additional time delay to reach the equilibrium. The heat flux generated at higher power levels (i.e. 0.64 W and 1W), was enough to rise the temperature of the heater above the melting point of the PCM. An increase in heat flux resulted in a faster melting while an increased amount of PCM increased the time delays. Figure 24.g compares the performances of graphene foam/silver as a heat sink in the horizontal and vertical configuration. The similar results obtained indicate the presence of convection in horizontal position and the validity of the approach for applications at a different orientation. Figure 24.h summarizes the time delays and the junctions temperatures corresponding to different power levels and weights of PCM.

3.3.2.2 Role of secondary microchannels in heat transfer

The heat transfer and fluid flow were modelled using the finite element method (FEM) software COMSOL Multiphysics v5.4 to identify the contribution of the secondary microchannels within the microporous 3D graphene foam. The case study is related to heat conduction in solid and fluid flow through the secondary microchannels, while the radiative heat transfer and the temperature dependence of other properties were neglected. A velocity of 0.1 m/s was forced in order to take into consideration the experiment conditions. Figure 25 present the schematic of the 3D and 2D single strute model.

Figure 26.a and 26.b show the 3D and 2D representations of the foam and joule heating results, respectively. While the highest temperature is achieved at the centre of the chip, the temperatures profile around the chip remains relatively high at equilibrium state. It indicates that good contact of the heat sink on the back of the chip is required in order to achieve good heat dissipation efficiency. Figure 27. (a-c) show the

results of velocity magnitudes, pressures and convective heat fluxes along a vertical column of the foam. Insets of each parameter are showed within its respective figure. The velocity of the air flow is seen decreasing more within the secondary microchan-

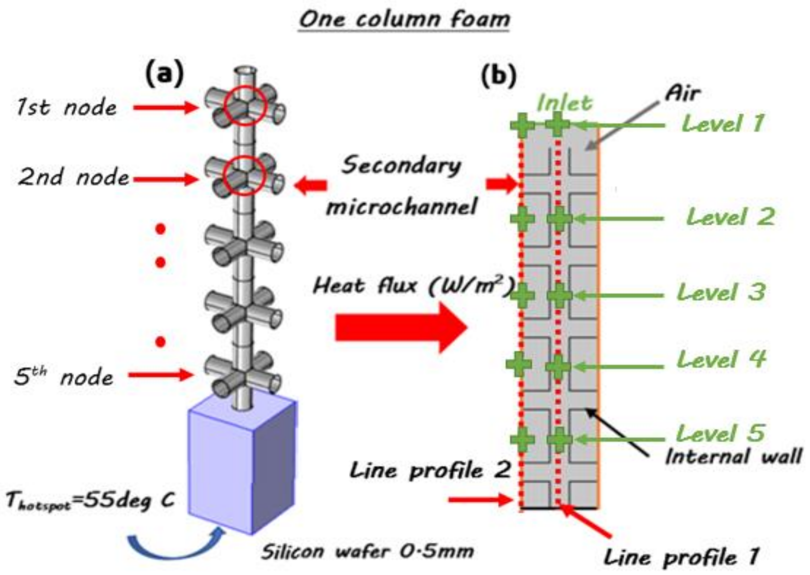

Figure 25: (a) 3D model of the one single column part of the foam with five nodes, (b) 2D representation of the single column foam with lines profiles and local levels indicated for the studied parameters.

nels comparatively to air flow within the primary microchannels. A pressure build-up is observed within the inner volume of the cylindrical column in results to the small diameters of the secondary microchannels. The convective heat flux follows the trend of the airflow velocities along the column, and a more significant decrease is observed within the column comparatively to the outer volume.

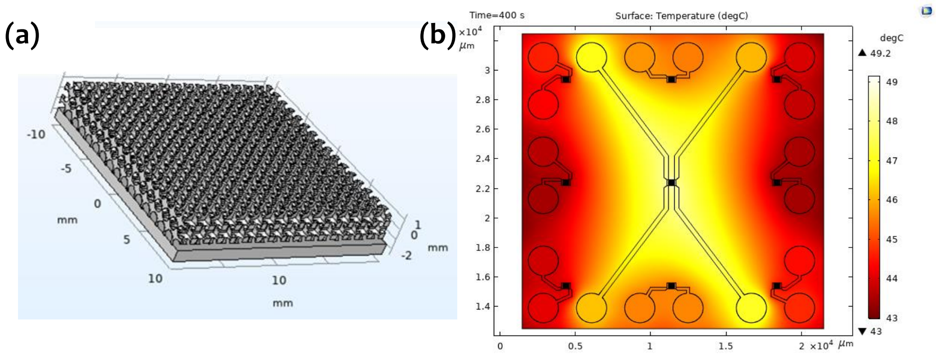

Figure 26: (a) 3D representation of the graphene foam deposited on the surface of the heater, (b) 2D result of the temperature profile on the side of the heater at 0.64W.

Figure 27.d shows the variation of velocity magnitude and convective heat flux along with the line profiles 1 and 2. For the secondary microchannels (line profile 1), the convective heat flux decreases gradually after each node along the vertical struts. In the case of the primary microchannels (line profile 2), the convective heat flux slowly decreases as the airflow is slowed down. The convective flux in the latter case is still comparable to the

convective flux within the primary microchannels and contributes to the overall heat exchange. Table 1 summarizes the values of the ratio between the airflow within the primary and the secondary microchannels at five different levels (see Figure 25).

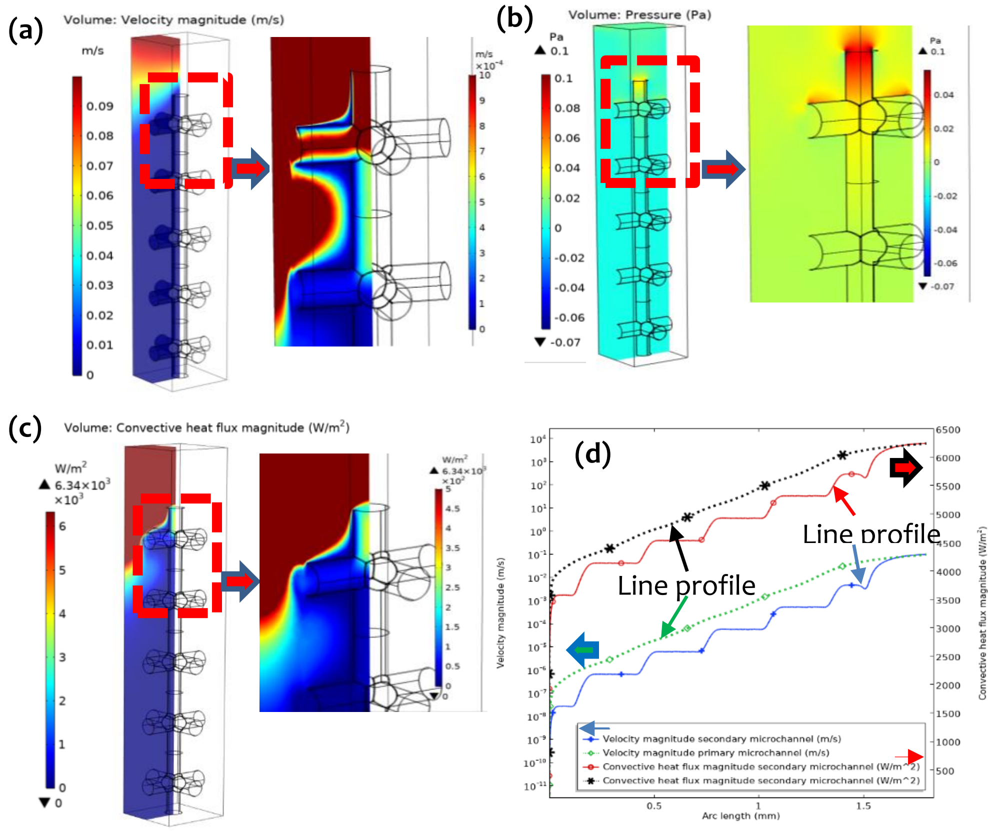

Figure 27: 3D profile showing the (a) velocity magnitude with an inset of the top of the foam with a maximum scale limited to 10 · 10⁻⁴ m/s, (b) pressure evolution along the vertical column with an inset of the top of the foam and a maximum scale limited to 0.1 Pa, (c) convective heat flux along the column with an inset of the top of the foam and a maximum scale limited to 5 · 10² W/m² (d) profiles of the air flow velocity and convective heat flux magnitudes along the primary and secondary microchannels in the

Table 4: Ratio values of velocity, pressure variation and convective heat flux magnitudes at five points along the foam column between the flow in the primary and secondary microchannels

	Velocity magnitude ratio	Pressure variation ratio	Convective heat flux ratio
Level 1	15,41	0,08	15,41
Level 2	10,61	0,20	10,61
Level 3	8,09	0,14	8,09
Level 4	6,50	0,12	6,50
Level 5	5,09	0,09	5,09

Chapter 4: Conclusion

This thesis aims at contributing in the development of nanomaterials for low-temperature sintering and thermal management through an effort to produce and characterize multi-element nanoparticles as a sintering aid for powder metallurgy and the use of the graphene material as a coating and 3D high porosity materials as a heat spreader for electronics cooling.

The first part of the thesis shows the result of the production and characterization of low carbon steel nanopowders as a multielement alloyed nanopowder. The morphological analysis showed the produced particles as nanosphere with an average size of 64nm. Smaller particles with sizes as small as few nanometers were also detected. Iron structure was identified with XRD analysis and a small fraction of iron oxide was detected and observed to surround the nanoparticle as a shell-core structure of iron oxide-iron. While the melting depression was found difficult to link directly to the size of the particle, the produced iron nanopowder showed an early shrinkage activation. Comparatively to previously reported work. In addition, a novel effect is reported as a self-reduction process due to the presence of carbon within the powder. Such properties indicate preliminary a composition effect that is combined with a size effect and can be used for applications in PM technologies. Additional effort to determine the local chemical composition within the nanoparticles is required in order to understand fully the effect of the alloying element in the densification of iron nanoparticles.

Graphene coated copper nanoparticles were developed in this work as fillers for water based nanofluids. The coated nanoparticles were found in the nanometer size range and fully covered with multilayers graphene that is assumed to act as a protective layer against the oxidation of the metallic nanoparticles in water. The evolution of the thermal properties of the nanofluid indicated a positive correlation with the increase of the concentration of the fillers. Such an increase is assumed to be due to the presence of the nanofillers with a high thermal conductivity that contributes to the thermal transport. In addition, the thermal conductivity of the fluids was found to increase with the increase of the temperature as a result of the increase in the mobility of the nanoparticles within the fluid through Brownian motion and nanoconvection. As a Newtonian fluidic system, the viscosity of the fluids was constant through the addition of different concentration of the nanoparticles except for high concentrations and low shear rate that were found to promote the segregation of the nanoparticles. The promising results shown by the graphene coated copper nanoparticles allow their use in electronics cooling as promising nanofillers. Additional work to study and improve the stability of the graphene coated nanoparticles is needed.

The graphene foam effective thermal conductivity was measured using DRT joule heating and a further 54% enhancement through the addition of a silver coating was achieved. Even though the thermal conductivity of the composite was found lower than that of pure copper, it is assumed that such structure can still be a good alternative for application in electronics where copper is not recommended. Further improvement of the thermal conductivity of the foam can be investigated by decreasing the graphene thickness in term of the number of layers and proceeding to heat treatments to improve the structural properties of the foam and enhance the thermal transport capabilities. The use of silver nanoparticles allowed achieving a good quality sintering at relatively low temperatures exploiting the mechanical flexibility of the graphene foam to achieve maximum surface contact with the substrate. As a result, the thermal properties of the graphene foam heat sink achieved better cooling performances in combination with the intrinsic high thermal conductivity of the graphene. The impregnation of the high latent energy organic material resulted in the slowdown of the temperature-rise considerably while showing a positive effect on reducing the maximum temperature. A CFD model was developed and showed that the additional secondary microchannels within the foam contribute to the heat transfer. Even though the conduction mode is dominating the heat transfer process in such systems, it was found that the secondary microchannels in the case of graphene foam-based approach can have a positive and non-negligible contribution in the heat transfer process. Therefore, the high porosity graphene foam gives a chance to the potential use of this system in advanced heat transfer strategies combining high conductivity material, high latent energy, and high convective heat flux approach.

Acknowledgments

"Knowledge is in the end based on acknowledgement", Ludwig Wittgenstein

This work would not have been achieved without the presence of valuable people who contributed with their time and effort. While this work is still to be completed with further effort, I would like to express first my gratitude through these words to my supervisor, Pr. Johan Liu, for the opportunity to be part of the electronics packaging group within the MC2 department and the effort to contain my education. My sincerest thanks go for my co-supervisor, Dr. Lilei, for the countless meetings and support I got from her. Honest thanks go also to Dr. Torbjörn Nilsson who has been closely involved in a part of this work and for his presence through the years.

I would like to acknowledge the help, assistance and shared time I got from my former and current colleagues within the EMSL and Chalmers: Andreas Nylander, Christian Chandra Darmawan, Hisham Aboulfadl, Josef Hansson, Marti Gutierrez Latorre, Michael Edwards, Nan Wang, Ning Wang, Peng Su, Shuangxi Sun, Vijayshankar Asokan, Wei Mu, Ya Liu, Yifei Zhang, Yifeng Fu and Yong Zhang. Also, I don't want to miss to grab the opportunity and thank every person involved in my presence, in a direct and indirect way within Chalmers University of Technology. A particular thought goes the staff at the MC2 department and Kaija Matikainen to whom I wish a delightful retirement.

A word of gratitude to the supervisors within the SSF project nanopowder enhanced sintering: Carin Andersson, Eduard Hryha, Lars Nyborg, Ulf Olofsson, Yu Cao, Åsa Rudolphi, and my PhD students colleagues: Anders Holmberg, Babak Kianian, Edwin Bergstedt, Johan Wendel, Maheswaran Vattur Sundaram, Swathi Kiranmayee Manchili.

My profound thought goes to my friends and family whom I could always count on their support: Amine Amirouche '3mimegh' for the valuable friendship and for solving the problems of the universe while still trying to go beyond; Nicolaos Logothetis 'Mouz bro' and Majid Samani Kabiri ' 😉 ' whose friendships survived the stress of the years with all the ups and the many downs; the other Greek guys, Dimitris, Kostas and Kuriakos with whom we could not escape the 'lab' room, but still find ways to escape the reality of life; Elise who has been part of a big part of this and Hadjer who is breaking bad.

This work was supported by the Swedish Foundation for Strategic Research (SSF) under contract No: GMT14-0045 and SE13-0061.

Hafid,

Göteborg, May 2020.

References

[1] I. Khan, K. Saeed, and I. Khan, “Nanoparticles: Properties, applications and toxicities,” *Arabian Journal of Chemistry*, vol. 12, no. 7. Elsevier B.V., pp. 908–931, 01-Nov-2019.

[2] D. Astruc, “Introduction: Nanoparticles in Catalysis,” *Chemical Reviews*, vol. 120, no. 2. American Chemical Society, pp. 461–463, 22-Jan-2020.

[3] S. Kiranmayee Manchili, “Role of nanopowder as sintering aid in the densification of water atomized ferrous powder,” Chalmers University of Technology, Gothenburg, 2018.

[4] M. Green, L. Tian, P. Xiang, J. Murowchick, X. Tan, and X. Chen, “FeP nanoparticles: A new material for microwave absorption,” *Mater. Chem. Front.*, vol. 2, no. 6, pp. 1119–1125, May 2018.

[5] T. Thu Trang Mai, P. Thu Ha, H. Nam Pham, and al -, “Magnetic fluid based on Fe3 O4 nanoparticles: Preparation and hyperthermia application,” *J. Phys. Conf. Ser*, vol. 187, p. 12069, 2009.

[6] K. Rajan, I. Roppolo, A. Chiappone, S. Bocchini, D. Perrone, and A. Chiolerio, “Silver nanoparticle ink technology: State of the art,” *Nanotechnology, Science and Applications*, vol. 9. Dove Medical Press Ltd, p. 1, 11-Jan-2016.

[7] C. Kleinstreuer and Y. Feng, “me,” *Nanoscale Research Letters*, vol. 6, no. 1. Springer New York LLC, p. 229, 16-Dec-2011.

[8] F. Gao and Z. Gu, “Melting temperature of metallic nanoparticles,” in *Handbook of Nanoparticles*, Springer International Publishing, 2015, pp. 661–690.

[9] M. J. Coutts, M. B. Cortie, M. J. Ford, and A. M. McDonagh, “Rapid and controllable sintering of gold nanoparticle inks at room temperature using a chemical agent,” *J. Phys. Chem. C*, vol. 113, no. 4, pp. 1325–1328, Jan. 2009.

[10] G. Vandevenne *et al.*, “A study on the thermal sintering process of silver nanoparticle inkjet inks to achieve smooth and highly conducting silver layers,” *Phys. status solidi*, vol. 213, no. 6, pp. 1403–1409, Jun. 2016.

[11] N. K. Roy *et al.*, “A comprehensive study of the sintering of copper nanoparticles using femtosecond, nanosecond, and continuous wave lasers,” *J. Micro Nano-Manufacturing*, vol. 6, no. 1, pp. 1–21, Mar. 2018.

[12] S. Divi and A. Chatterjee, “Generalized nano-thermodynamic model for capturing size-dependent surface segregation in multi-metal alloy nanoparticles,” *RSC Adv.*, vol. 8, no. 19, pp. 10409–10424, Mar. 2018.

[13] R. Ferrando, R. L. Johnston, and C. Louis, “Recent advances in the chemical physics of nanoalloys,” *Physical Chemistry Chemical Physics*, vol. 17, no. 42, Royal Society of Chemistry, pp. 27920–27921, 2015.

[14] A. V. Samokhin, N. V. Alexeev, A. A. Fadeev, and Y. V. Tsvetkov, "Formation of nanoparticles of binary W-Cu and ternary W-Ni-Fe systems in thermal plasma jet," 2013, pp. 2P-167-2P – 167.

[15] J. Y. Huh, H. Lee, and W. C. Johnson, "Particle size effects on the coherent phase equilibria of binary nanoparticles," *Met. Mater. Int.*, vol. 11, no. 5, pp. 357–363, 2005.

[16] A. A. Baqer *et al.*, "Synthesis and characterization of binary (CuO)0.6(CeO2)0.4 nanoparticles via a simple heat treatment method," *Results Phys.*, vol. 9, pp. 471–478, Jun. 2018.

[17] K. C. Pingali, S. Deng, and D. A. Rockstraw, "DIRECT SYNTHESIS OF RU-NI NANOPARTICLES WITH CORE-AND-SHELL STRUCTURE," *Chem. Eng. Commun.*, vol. 194, no. 6, pp. 780–786, Mar. 2007.

[18] M. Benelmekki and M. Benelmekki, "Designing binary nanoparticles," in *Designing Hybrid Nanoparticles*, Morgan & Claypool Publishers, 2014.

[19] G. Barcaro, L. Sementa, and A. Fortunelli, "Nano (Evanescent-Wave)-Particle Image Velocimetry Nanoalloy Simulation," 2016.

[20] V. M. Samsonov, I. V. Talyzin, A. Y. Kartoshkin, and S. A. Vasilyev, "Surface segregation in binary Cu–Ni and Au–Co nanoalloys and the core–shell structure stability/instability: thermodynamic and atomistic simulations," *Appl. Nanosci.*, vol. 9, no. 1, pp. 119–133, Feb. 2019.

[21] M. Cui, H. Lu, H. Jiang, Z. Cao, and X. Meng, "Phase Diagram of Continuous Binary Nanoalloys: Size, Shape, and Segregation Effects OPEN," *Nat. Publ. Gr.*, 2017.

[22] L. A. Jauregui *et al.*, "Thermal Transport in Graphene Nanostructures: Experiments and Simulations," in *ECS Transactions*, 2010, vol. 28, no. 5, pp. 73–83.

[23] R. Taylor *et al.*, "Small particles, big impacts: A review of the diverse applications of nanofluids ," *J. Appl. Phys*, vol. 113, p. 11301, 2013.

[24] M. Vattur Sundaram, "Novel approaches for achieving full density powder metallurgy steels," CHALMERS UNIVERSITY OF TECHNOLOGY, Gothenburg, 2019.

[25] R. M. German, "Thermodynamics of sintering," in *Sintering of Advanced Materials*, Elsevier, 2010, pp. 3–32.

[26] E. A. Olevsky, "Theory of sintering: From discrete to continuum," *Mater. Sci. Eng. R Reports*, vol. 23, no. 2, pp. 41–100, Jun. 1998.

[27] M. N. Rahaman, "Sintering Theory and Fundamentals," in *Powder Metallurgy*, ASM International, 2018, pp. 205–236.

[28] T. T. Molla, "Modeling Macroscopic Shape Distortions during Sintering of Multi-layers Modeling Macroscopic Shape Distortions during Sintering of Multi-layers By : Tesfaye Tadesse Molla," Technical University of Danmark, 2016.

[29] Z. H. Li and D. Truhlar, "Nanothermodynamics of Metal Nanoparticles Chemical Science Nanothermodynamics of metal nanoparticles," no. March 2016, 2014.

[30] M. Ghasemi, Z. Zanolli, M. Stankovski, and J. Johansson, "Size- and shape-dependent phase diagram of In-Sb nano-alloys," *Nanoscale*, vol. 7, no. 41, pp. 17387–17396, Nov. 2015.

[31] J. Sopoušek *et al.*, "Au-Ni nanoparticles: Phase diagram prediction, synthesis, characterization, and thermal stability," *Calphad Comput. Coupling Phase Diagrams Thermochem.*, vol. 58, pp. 25–33, Sep. 2017.

[32] M. Wautelet, J. P. Dauchot, and M. Hecq, "Size effects on the phase diagrams of nanoparticles of various shapes," *Mater. Sci. Eng. C*, vol. 23, no. 1–2, pp. 187–190, Jan. 2003.

[33] F. Calvo, *Nanoalloys - From Fundamentals to Emergent Applications*, Elsevier. 2013.

[34] A. Voloshko, "Nanoparticle formation by means of spark discharge at atmospheric pressure," Université Jean Monnet - Saint-Etienne, 2015.

[35] A. Safaei, M. Attarian Shandiz, S. Sanjabi, and Z. H. Barber, "Modeling the melting temperature of nanoparticles by an analytical approach," *J. Phys. Chem. C*, vol. 112, no. 1, pp. 99–105, Jan. 2008.

[36] Y. S. Kaganovskii and L. N. Paritskaya, "Size-Dependent Effects in Low-Temperature Sintering and Alloying of Nanopowders," *Powder Metall. Met. Ceram.*, vol. 57, no. 7–8, pp. 421–430, Nov. 2018.

[37] G. Guenther and O. Guillon, "Models of size-dependent nanoparticle melting tested on gold," *Journal of Materials Science*, vol. 49, no. 23. Kluwer Academic Publishers, pp. 7915–7932, 01-Dec-2014.

[38] F. Font and T. G. Myers, "Spherically symmetric nanoparticle melting with a variable phase change temperature," 2013.

[39] D. Feng, Y. Feng, S. Yuan, X. Zhang, and G. Wang, "Melting behavior of Ag nanoparticles and their clusters," *Appl. Therm. Eng.*, vol. 111, pp. 1457–1463, Jan. 2017.

[40] D. Feng, Y. Feng, S. Yuan, X. Zhang, and G. Wang, *Handbook of Mechanical Nanostructuring*, John Wiley & Sons., vol. 1. John Wiley & Sons, 2015.

[41] Q. Mao, Y. Ren, K. H. Luo, and S. Li, "Sintering Induced Phase Transformation of Nanoparticles: A Molecular Dynamics Study."

[42] J.-H. Yu, C.-S. Youn, B.-K. Kim, J.-S. Lee, and C.-J. Choi, "Characteristics and

Sintering Behavior of Oxide Coated Iron Nanopowder Synthesized by Plasma Arc Discharge Process."

[43] M. Terrones *et al.*, "Graphene and graphite nanoribbons: Morphology, properties, synthesis, defects and applications," *Nano Today*, vol. 5, no. 4. Elsevier B.V., pp. 351–372, 2010.

[44] Y. Y. Zhang and Y. T. Gu, "Mechanical properties of graphene: Effects of layer number, temperature and isotope," *Comput. Mater. Sci.*, vol. 71, pp. 197–200, Apr. 2013.

[45] Y. W. Sun *et al.*, "3D Strain in 2D Materials: To What Extent is Monolayer Graphene Graphite?," *Phys. Rev. Lett.*, vol. 123, 2019.

[46] G. Yang, L. Li, W. B. Lee, and M. C. Ng, "Structure of graphene and its disorders: a review," *Science and Technology of Advanced Materials*, vol. 19, no. 1. Taylor and Francis Ltd., pp. 613–648, 31-Dec-2018.

[47] Y. Shan *et al.*, "Stacking symmetry governed second harmonic generation in graphene trilayers," 2018.

[48] L. Zhong *et al.*, "Unraveling the Influence of Metal Substrates on Graphene Nucleation from First-Principles Study," *J. Phys. Chem. C*, vol. 120, no. 40, pp. 23239–23245, Oct. 2016.

[49] M. Batzill, "The surface science of graphene: Metal interfaces, CVD synthesis, nanoribbons, chemical modifications, and defects," *Surf. Sci. Rep.*, vol. 67, pp. 83–115, 2012.

[50] G. Zhao *et al.*, "The physics and chemistry of graphene-on-surfaces," *Chemical Society Reviews*, vol. 46, no. 15. Royal Society of Chemistry, pp. 4417–4449, 07-Aug-2017.

[51] A. Dahal, R. Addou, H. Coy-Diaz, J. Lallo, and M. Batzill, "Charge doping of graphene in metal/graphene/dielectric sandwich structures evaluated by C-1s core level photoemission spectroscopy," *APL Mater.*, vol. 1, no. 4, p. 042107, Oct. 2013.

[52] X. Zhang, H. Li, and F. Ding, "Self-Assembly of Carbon Atoms on Transition Metal Surfaces-Chemical Vapor Deposition Growth Mechanism of Graphene," *Adv. Mater.*, vol. 26, no. 31, pp. 5488–5495, Aug. 2014.

[53] T. P. Sarit K. Das, Stephen U. Choi, Wenhua Yu, *Nanofluids: Science and Technology*, December 2. Wiley, 2554.

[54] M. R. Rodríguez-Laguna *et al.*, "Mechanisms behind the enhancement of thermal properties of graphene nanofluids †," vol. 10, p. 15402, 2018.

[55] M. Loeblein *et al.*, "High-Density 3D-Boron Nitride and 3D-Graphene for High-Performance Nano-Thermal Interface Material," *ACS Nano*, vol. 11, no. 2, pp. 2033–2044, Feb. 2017.

[56] M. Loeblein, R. Y. Tay, S. H. Tsang, W. B. Ng, and E. H. T. Teo, "Configurable three-dimensional boron nitride-carbon architecture and its tunable electronic behavior with stable thermal performances," *Small*, vol. 10, no. 15, pp. 2992–2999, 2014.

[57] M. Loeblein *et al.*, "3D Graphene-Infused Polyimide with Enhanced Electrothermal Performance for Long-Term Flexible Space Applications," *Small*, vol. 11, no. 48, pp. 6425–6434, Dec. 2015.

[58] M. T. Pettes, H. Ji, R. S. Ruoff, and L. Shi, "Thermal transport in three-dimensional foam architectures of few-layer graphene and ultrathin graphite," *Nano Lett.*, vol. 12, no. 6, pp. 2959–2964, Jun. 2012.

[59] J. W. Klett, A. D. McMillan, N. C. Gallego, and C. A. Walls, "The role of structure on the thermal properties of graphitic foams," *J. Mater. Sci.*, vol. 39, no. 11, pp. 3659–3676, Jun. 2004.

[60] Z. Yan, D. L. Nika, and A. A. Balandin, "Review of Thermal Properties of Graphene and Few-Layer Graphene: Applications in Electronics."

[61] K. Lafdi, M. Almajali, and O. Huzayyin, "Thermal properties of copper-coated carbon foams," *Carbon N. Y.*, vol. 47, no. 11, pp. 2620–2626, Sep. 2009.

[62] S. M. Sadrameli, F. Motaharinejad, M. Mohammadpour, and F. Dorkoosh, "An experimental investigation to the thermal conductivity enhancement of paraffin wax as a phase change material using diamond nanoparticles as a promoting factor," *Heat Mass Transf. und Stoffuebertragung*, vol. 55, no. 6, pp. 1801–1808, Jun. 2019.

[63] M. Karkri, M. Lachheb, D. Gossard, S. Ben Nasrallah, and M. A. Almaadeed, "Improvement of thermal conductivity of paraffin by adding expanded graphite."

[64] D. Li *et al.*, "Measuring Thermal and Thermoelectric Properties of One-Dimensional Nanostructures Using a Microfabricated Device," 2003.

[65] Z. Chen, D. Gao, and J. Shi, "Experimental and numerical study on melting of phase change materials in metal foams at pore scale," *Int. J. Heat Mass Transf.*, vol. 72, pp. 646–655, May 2014.

[66] E. Fleming, S. Wen, L. Shi, and A. K. Da Silva, "Experimental and theoretical analysis of an aluminum foam enhanced phase change thermal storage unit," *Int. J. Heat Mass Transf.*, vol. 82, pp. 273–281, 2015.

[67] Z. Zhang and Y. Li, "Experimental study of a passive thermal management system using copper foam-paraffin composite for lithium ion batteries," in *Energy Procedia*, 2017, vol. 142, pp. 2403–2408.

[68] Z. Wang, Z. Zhang, L. Jia, and L. Yang, "Paraffin and paraffin/aluminum foam composite phase change material heat storage experimental study based on

thermal management of Li-ion battery," *Appl. Therm. Eng.*, vol. 78, pp. 428–436, Mar. 2015.

[69] A. Hussain, C. Y. Tso, and C. Y. H. Chao, "Experimental investigation of a passive thermal management system for high-powered lithium ion batteries using nickel foam-paraffin composite," *Energy*, vol. 115, pp. 209–218, Nov. 2016.

[70] A. Hussain, I. H. Abidi, C. Y. Tso, K. C. Chan, Z. Luo, and C. Y. H. Chao, "Thermal management of lithium ion batteries using graphene coated nickel foam saturated with phase change materials," *Int. J. Therm. Sci.*, vol. 124, pp. 23–35, Feb. 2018.